

Gluino Decays in the Complex MSSM: A Full One-Loop Analysis

S. HEINEMEYER^{1*} AND C. SCHAPPACHER^{2†}

¹*Instituto de Física de Cantabria (CSIC-UC), Santander, Spain*

²*Institut für Theoretische Physik, Karlsruhe Institute of Technology,
D-76128 Karlsruhe, Germany*

Abstract

We evaluate all two-body decay modes of the gluino, in the Minimal Supersymmetric Standard Model with complex parameters (cMSSM). This constitutes an important step in the cascade decays of SUSY particles at the LHC. The evaluation is based on a full one-loop calculation of all two-body decay channels, also including hard QED and QCD radiation. The dependence of the gluino decay to a scalar quark and a quark on the relevant cMSSM parameters is analyzed numerically. We find sizable contributions to the decay widths and branching ratios. They are, roughly of $\mathcal{O}(\pm 5\%)$, but can go up to $\pm 10\%$ or higher, where the pure SUSY QCD contributions alone can give an insufficient approximation to the full one-loop result. Therefore the full corrections are important for the correct interpretation of gluino decays at the LHC. The results will be implemented into the Fortran code `FeynHiggs`.

*email: Sven.Heinemeyer@cern.ch

†email: cs@particle.uni-karlsruhe.de

1 Introduction

One of the most important tasks at the LHC is to search for physics effects beyond the Standard Model (SM), where the Minimal Supersymmetric Standard Model (MSSM) [1] is one of the leading candidates. Supersymmetry (SUSY) predicts two scalar partners for all SM fermions as well as fermionic partners to all SM bosons. Especially it predicts the fermionic gluino as a superpartner of the bosonic gluon.

If SUSY is realized in nature and the gluino and/or scalar quarks are in the kinematic reach of the LHC, it is expected that these strongly interacting particles are copiously produced Refs. [2,3]. After the (pair) production of these particles they are expected to decay via cascades to lighter SUSY particles and quarks and/or leptons. Many models predict that the heaviest SUSY particle is indeed the gluino (see, for instance, Ref. [4] and references therein), and consequently, the decay to a scalar quark and a quark will one of the most relevant decays in such a cascade. Only if these two-body decays are kinematically forbidden other decay channels can become numerically relevant. These are either two-body decays that are purely loop-induced, or three-body decays via a virtual squark. In this paper we will concentrate on the two-body decays that are allowed at tree-level already. We will also, for the sake of completeness, evaluate the two-body decays that appear only at the loop-level, the decays of the gluino to a gluon and a neutralino, which can potentially serve as a production source of the cMSSM cold dark matter (CDM) candidate.

In order to yield a sufficient accuracy one-loop corrections to the various gluino decay modes have to be considered. As outlined above, we take into account all two-body decay modes of the gluino in the MSSM with complex parameters (cMSSM). More specifically we calculate the full one-loop corrections to

$$\Gamma(\tilde{g} \rightarrow \tilde{q}_i^\dagger q) \quad (i = 1, 2; q = t, b, c, s, u, d) , \quad (1)$$

$$\Gamma(\tilde{g} \rightarrow \tilde{q}_i \bar{q}) \quad (i = 1, 2; q = t, b, c, s, u, d) , \quad (2)$$

$$\Gamma(\tilde{g} \rightarrow \tilde{\chi}_k^0 g) \quad (k = 1, 2, 3, 4) . \quad (3)$$

A difference between $\Gamma(\tilde{g} \rightarrow \tilde{q}_i^\dagger q)$ and $\Gamma(\tilde{g} \rightarrow \tilde{q}_i \bar{q})$ can arise from complex parameters. In the case when all parameters are real (and sometimes to simplify the notation) we also use the notation $\Gamma(\tilde{g} \rightarrow \tilde{q}_i q)$ referring to *both* channels. The total width is defined as the sum of the channels (1) – (3), where for a given parameter point several of the 28 channels may be kinematically forbidden. As it is expected, the channel (3) is numerically irrelevant for the total width as long as one or more of the two-body tree-level decays is kinematically allowed.

One-loop QCD corrections to gluino decays have been evaluated in Ref. [5]. The calculation was done in the MSSM with real parameters (rMSSM). Those $\mathcal{O}(\alpha_s)$ corrections have been implemented into the code `SDECAY` [6]. To our knowledge, no evaluation of electroweak (EW) corrections to gluino decays, nor any higher-order corrections involving complex phases have been performed so far. Gluino decays at the tree-level were employed, for instance, in Ref. [7] to determine their Majorana/Dirac character. Gluino polarizations were analyzed in Ref. [8]. Again, both analyses were performed in the rMSSM.

Several methods have been discussed in the literature to extract the complex parameters of the model from experimental measurements. However, no such an analysis, to our knowledge, of the phase of the gluino mass parameter, M_3 , has been performed so far. We analyze

the effects of this phase on the branching ratios (BR's) of the gluino, also as a motivation to devise experimental strategies to determine this parameter at the LHC (or other future colliders) [9].

In this paper we present for the first time a full one-loop calculation, including electroweak effects, for all two-body decay channels of the gluino in the cMSSM. The calculation includes soft and hard QED and QCD radiation. In Sect. 2 we review the relevant sectors of the cMSSM. Details about the calculation can be found in Sect. 3, and the numerical results for all decay channels are presented in Sect. 4, where we discuss especially the size of the EW corrections and the effects from the complex gluino phase. The conclusions can be found in Sect. 5. The evaluation of the branching ratios of the gluino will be implemented into the Fortran code `FeynHiggs` [10–13].

2 The relevant sectors of the complex MSSM

All the channels (1) – (3) are calculated at the one-loop level, including hard QED and QCD radiation (for the decays that exist already at the tree-level). This requires the simultaneous renormalization of several sectors of the cMSSM, where details can be found in Refs. [14–16]. In the following subsections we briefly review these relevant sectors.

2.1 The squark sector of the cMSSM

For the evaluation of the one-loop contributions to the decay of the \tilde{g} to a squark and quark, a renormalization of the scalar quark sector is needed. The squark mass matrix $\mathbf{M}_{\tilde{q}}$ read

$$\mathbf{M}_{\tilde{q}} = \begin{pmatrix} M_{\tilde{q}L}^2 + m_q^2 + M_Z^2 (I_q^3 - Q_q s_w^2) \cos 2\beta & m_q X_q^* \\ m_q X_q & M_{\tilde{q}R}^2 + m_q^2 + M_Z^2 Q_q s_w^2 \cos 2\beta \end{pmatrix} \quad (4)$$

with

$$X_q = A_q - \mu^* \kappa, \quad \kappa = \{\cot \beta, \tan \beta\} \quad \text{for } q = \{u\text{-type}, d\text{-type}\}. \quad (5)$$

$M_{\tilde{q}L}$ and $M_{\tilde{q}R}$ are the soft SUSY-breaking mass parameters, where $M_{\tilde{q}L}$ is equal for all members of an $SU(2)_L$ doublet and $M_{\tilde{q}R}$ depends on the scalar quark flavor. m_q is the mass of the corresponding quark. Q_q and I_q^3 denote the charge and isospin of q , and A_q is the trilinear soft-breaking parameter. M_Z and M_W are the masses of the Z and W boson, $c_w = M_W/M_Z$, and $s_w = \sqrt{1 - c_w^2}$. The mass matrix can be diagonalized with the help of a unitary transformation $\mathbf{U}_{\tilde{q}}$,

$$\mathbf{D}_{\tilde{q}} = \mathbf{U}_{\tilde{q}} \mathbf{M}_{\tilde{q}} \mathbf{U}_{\tilde{q}}^\dagger = \begin{pmatrix} m_{\tilde{q}1}^2 & 0 \\ 0 & m_{\tilde{q}2}^2 \end{pmatrix}, \quad \mathbf{U}_{\tilde{q}} = \begin{pmatrix} U_{\tilde{q}11} & U_{\tilde{q}12} \\ U_{\tilde{q}21} & U_{\tilde{q}22} \end{pmatrix}. \quad (6)$$

The mass eigenvalues depend only on $|X_q|$. The scalar quark masses will always be mass ordered, i.e. $m_{\tilde{q}1} \leq m_{\tilde{q}2}$:

$$m_{\tilde{q}1,2}^2 = \frac{1}{2} (M_{\tilde{q}L}^2 + M_{\tilde{q}R}^2) + m_q^2 + \frac{1}{2} I_q^3 M_Z^2 \cos 2\beta$$

$$\mp \frac{1}{2} \sqrt{[M_{\tilde{q}_L}^2 - M_{\tilde{q}_R}^2 + M_Z^2 (I_q^3 - 2Q_q s_w^2) \cos 2\beta]^2 + 4m_q^2 |X_q|^2} . \quad (7)$$

Details about the renormalization of the scalar quark sector of the cMSSM can be found in Refs. [15, 16]. The employed renormalization preserves the $SU(2)_L$ symmetry of the model. It is ensured that all external particles fulfill the required on-shell (OS) properties for masses and Z factors. The field renormalization requires the renormalization of the off-diagonal entry in the squark mass matrix, which leads to a renormalization of the trilinear couplings A_q , μ and $\tan \beta$, see below. It was shown in Refs. [15, 16] that the renormalization produces stable and well-behaved results for nearly the whole cMSSM parameter space.

Finally it should be noted that we take into account the absorptive part of the self-energy type contributions on the external legs via combined Z factors which are different for incoming squarks/outgoing antisquarks (unbarred) and outgoing squarks/incoming antisquarks (barred) [16]:

(i) The diagonal Z factors read

$$[\delta \mathcal{Z}_{\tilde{q}}]_{ii} = [\delta \bar{\mathcal{Z}}_{\tilde{q}}]_{ii} = -\Sigma'_{\tilde{q}ii}(m_{\tilde{q}_i}^2) \quad (i = 1, 2) . \quad (8)$$

(ii) The off-diagonal Z factors read

$$[\delta \mathcal{Z}_{\tilde{q}}]_{12} = +2 \frac{\Sigma_{\tilde{q}_{12}}(m_{\tilde{q}_2}^2) - \delta Y_q}{(m_{\tilde{q}_1}^2 - m_{\tilde{q}_2}^2)} , \quad [\delta \mathcal{Z}_{\tilde{q}}]_{21} = -2 \frac{\Sigma_{\tilde{q}_{21}}(m_{\tilde{q}_1}^2) - \delta Y_q^*}{(m_{\tilde{q}_1}^2 - m_{\tilde{q}_2}^2)} , \quad (9)$$

$$[\delta \bar{\mathcal{Z}}_{\tilde{q}}]_{12} = +2 \frac{\Sigma_{\tilde{q}_{21}}(m_{\tilde{q}_2}^2) - \delta Y_q^*}{(m_{\tilde{q}_1}^2 - m_{\tilde{q}_2}^2)} , \quad [\delta \bar{\mathcal{Z}}_{\tilde{q}}]_{21} = -2 \frac{\Sigma_{\tilde{q}_{12}}(m_{\tilde{q}_1}^2) - \delta Y_q}{(m_{\tilde{q}_1}^2 - m_{\tilde{q}_2}^2)} . \quad (10)$$

$\Sigma_{\tilde{q}_{ij}}$ denotes the scalar quark self-energies, and $\Sigma'(m^2) \equiv \frac{\partial \Sigma(p^2)}{\partial p^2} \Big|_{p^2=m^2}$. See Ref. [16] for the other renormalization constants and further details.

2.2 The quark sector of the cMSSM

In this section we briefly describe the quark sector of the cMSSM and its renormalization, extending the corresponding discussions in Refs. [15–17]. The quark mass, m_q , and the quark fields q_L, q_R are renormalized in the following way:

$$m_q \rightarrow m_q + \delta m_q , \quad (11)$$

$$q_{L/R} \rightarrow (1 + \frac{1}{2} \delta \mathcal{Z}_q^{L/R}) q_{L/R} , \quad (12)$$

$$\bar{q}_{L/R} \rightarrow (1 + \frac{1}{2} \delta \bar{\mathcal{Z}}_q^{L/R}) \bar{q}_{L/R} , \quad (13)$$

with δm_q being the quark mass counterterm and $\delta \mathcal{Z}_q^{L/R}$ being the combined Z factors of the left/right-handed quark fields, respectively. They are determined separately to include effects from the absorptive parts of the self-energy type contribution on an external quark leg [16]. The unbarred quantities denote incoming quarks/outgoing antiquarks and the barred denote outgoing quarks/incoming antiquarks. The renormalized self energy, $\hat{\Sigma}_q$, can be decomposed into left/right-handed and scalar left/right-handed parts, $\Sigma_q^{L/R}$ and $\Sigma_q^{SL/SR}$, respectively,

$$\hat{\Sigma}_q(p) = \not{p} \omega_- \hat{\Sigma}_q^L(p^2) + \not{p} \omega_+ \hat{\Sigma}_q^R(p^2) + \omega_- \hat{\Sigma}_q^{SL}(p^2) + \omega_+ \hat{\Sigma}_q^{SR}(p^2) , \quad (14)$$

where the components are given by

$$\hat{\Sigma}_q^{L/R}(p^2) = \Sigma_q^{L/R}(p^2) + \frac{1}{2}(\delta\mathcal{Z}_q^{L/R} + \delta\bar{\mathcal{Z}}_q^{L/R}) , \quad (15)$$

$$\hat{\Sigma}_q^{SL}(p^2) = \Sigma_q^{SL}(p^2) - \frac{m_q}{2}(\delta\mathcal{Z}_q^L + \delta\bar{\mathcal{Z}}_q^R) - \delta m_q , \quad (16)$$

$$\hat{\Sigma}_q^{SR}(p^2) = \Sigma_q^{SR}(p^2) - \frac{m_q}{2}(\delta\mathcal{Z}_q^R + \delta\bar{\mathcal{Z}}_q^L) - \delta m_q , \quad (17)$$

and $\omega_{\pm} = \frac{1}{2}(1 \pm \gamma_5)$ are the right- and left-handed projectors, respectively.

The quark mass is defined on-shell [18], yielding the one-loop counterterm δm_q :

$$\delta m_q^{\text{OS}} = \frac{1}{2}\widetilde{\text{Re}} \{ m_q [\Sigma_q^L(m_q^2) + \Sigma_q^R(m_q^2)] + [\Sigma_q^{SL}(m_q^2) + \Sigma_q^{SR}(m_q^2)] \} , \quad (18)$$

referring to the Lorentz decomposition of the self energy $\hat{\Sigma}_q(p)$, see Eq. (14). $\widetilde{\text{Re}}$ denotes the real part with respect to contributions from the loop integral, but leaves the complex couplings unaffected.

Special care is needed for the bottom sector due to potentially large effects at large $\tan\beta$ (denoting the ratio of the two vacuum expectation values). If (and only if) there are no external bottom quarks, the bottom-quark mass is defined $\overline{\text{DR}}$ (see Ref. [16] for more details), yielding the one-loop counterterm $\delta m_b^{\overline{\text{DR}}}$:

$$\delta m_b^{\overline{\text{DR}}} = \frac{1}{2}\widetilde{\text{Re}} \{ m_b [\Sigma_b^L(m_b^2) + \Sigma_b^R(m_b^2)]_{\text{div}} + [\Sigma_b^{SL}(m_b^2) + \Sigma_b^{SR}(m_b^2)]_{\text{div}} \} . \quad (19)$$

The new (diagonal) field renormalization constants, taking into account the absorptive part of the self-energy type contribution on an external quark leg are different for incoming quarks/outgoing antiquarks (unbarred) and outgoing quarks/incoming antiquarks (barred),

$$\begin{aligned} \delta\mathcal{Z}_q^{L/R} &= - \left[\Sigma_q^{L/R}(m_q^2) + m_q^2 \left(\Sigma_q^{L'}(m_q^2) + \Sigma_q^{R'}(m_q^2) \right) + m_q \left(\Sigma_q^{SL'}(m_q^2) + \Sigma_q^{SR'}(m_q^2) \right) \right] \\ &\quad \pm \frac{1}{2m_q} [\Sigma_q^{SL}(m_q^2) - \Sigma_q^{SR}(m_q^2)] , \end{aligned} \quad (20)$$

$$\begin{aligned} \delta\bar{\mathcal{Z}}_q^{L/R} &= - \left[\Sigma_q^{L/R}(m_q^2) + m_q^2 \left(\Sigma_q^{L'}(m_q^2) + \Sigma_q^{R'}(m_q^2) \right) + m_q \left(\Sigma_q^{SL'}(m_q^2) + \Sigma_q^{SR'}(m_q^2) \right) \right] \\ &\quad \mp \frac{1}{2m_q} [\Sigma_q^{SL}(m_q^2) - \Sigma_q^{SR}(m_q^2)] . \end{aligned} \quad (21)$$

For further details see Ref. [16].

The input parameters in the b sector have to correspond to the chosen renormalization. We start by defining the bottom mass, where the experimental input is the SM $\overline{\text{MS}}$ mass [19]. The value of $m_b^{\overline{\text{MS}}}(\mu_R)$ (at the renormalization scale μ_R) is calculated from $m_b^{\overline{\text{MS}}}(m_b)$ at the three loop level following the prescription given in Ref. [20]. The input parameters can be found in Sect. 4.1. The ‘‘on-shell’’ mass is connected to the $\overline{\text{MS}}$ mass via

$$m_b^{\text{OS}} = m_b^{\overline{\text{MS}}}(\mu_R) \left[1 + \frac{\alpha_s^{\overline{\text{MS}}}(\mu_R)}{\pi} \left(\frac{4}{3} + 2 \ln \frac{\mu_R}{m_b^{\overline{\text{MS}}}(\mu_R)} \right) \right] . \quad (22)$$

The $\overline{\text{DR}}$ bottom quark mass is calculated iteratively from

$$m_b^{\overline{\text{DR}}} = \frac{m_b^{\text{OS}}|1 + \Delta_b| + \delta m_b^{\text{OS}} - \delta m_b^{\overline{\text{DR}}}}{|1 + \Delta_b|} \quad (23)$$

with an accuracy of $|1 - (m_b^{\overline{\text{DR}}})^{(n)} / (m_b^{\overline{\text{DR}}})^{(n-1)}| < 10^{-5}$ reached in the n th step of the iteration and δm_b^{OS} as given in Eq. (18) with $q = b$. The quantity Δ_b [21,22] resums the $\mathcal{O}((\alpha_s \tan \beta)^n)$ and $\mathcal{O}(\alpha_t \tan \beta)^n$ terms and is given in Eq. (66) of Ref. [16].

In the case of external bottom quarks we use an OS renormalization scheme for the bottom sector. The bottom quark mass is then obtained from

$$m_b^{\text{OS}} = m_b^{\overline{\text{DR}}} + \delta m_b^{\overline{\text{DR}}} - \delta m_b^{\text{OS}} , \quad (24)$$

again with δm_b^{OS} from Eq. (18) with $q = b$.

2.3 The gluino and the strong coupling constant

The soft-breaking gluino mass parameter M_3 is in general complex,

$$M_3 = |M_3| e^{i\varphi_{\tilde{g}}} \quad (\text{with the gluino mass } m_{\tilde{g}} = |M_3|) . \quad (25)$$

We choose an OS renormalization for the gluino, where the renormalization constants can be found in Ref. [16]. It properly takes into account the complex phase of M_3 and yields an on-shell gluino, as it is required for an external particle in our decays.¹ It is possible to modify the field renormalization constants to take into account the absorptive part of the self-energy type contribution on the external gluino leg. The renormalization constants then read [16] (unbarred (barred) for an incoming (outgoing) gluino),

$$\delta M_3 = \frac{1}{2} \widetilde{\text{Re}} \{ m_{\tilde{g}} [\Sigma_{\tilde{g}}^L(m_{\tilde{g}}^2) + \Sigma_{\tilde{g}}^R(m_{\tilde{g}}^2)] + [\Sigma_{\tilde{g}}^{SL}(m_{\tilde{g}}^2) + \Sigma_{\tilde{g}}^{SR}(m_{\tilde{g}}^2)] \} e^{i\varphi_{\tilde{g}}} , \quad (26)$$

$$\begin{aligned} \delta \mathcal{Z}_{\tilde{g}}^{L/R} = & - \left[\Sigma_{\tilde{g}}^{L/R}(m_{\tilde{g}}^2) + m_{\tilde{g}}^2 \left(\Sigma_{\tilde{g}}^{L'}(m_{\tilde{g}}^2) + \Sigma_{\tilde{g}}^{R'}(m_{\tilde{g}}^2) \right) + m_{\tilde{g}} \left(\Sigma_{\tilde{g}}^{SL'}(m_{\tilde{g}}^2) + \Sigma_{\tilde{g}}^{SR'}(m_{\tilde{g}}^2) \right) \right] \\ & \pm \frac{1}{2m_{\tilde{g}}} [\Sigma_{\tilde{g}}^{SL}(m_{\tilde{g}}^2) - \Sigma_{\tilde{g}}^{SR}(m_{\tilde{g}}^2)] , \end{aligned} \quad (27)$$

$$\delta \bar{\mathcal{Z}}_{\tilde{g}}^{L/R} = \delta \mathcal{Z}_{\tilde{g}}^{R/L} . \quad (28)$$

The last formula holds due to the Majorana character of the gluino and we have chosen $\delta\varphi_{\tilde{g}} = 0$. This choice is possible, since the imaginary part of M_3 does not contain any divergence.²

Our renormalization of the strong coupling constant, α_s , is described in Refs. [14–16] (and references therein). The decoupling of the heavy particles is taken into account in the definition of α_s : Starting point is $\alpha_s^{\overline{\text{MS}}}(M_Z)$ [19], where the running can also be found in

¹ The general renormalization procedure is described in Refs. [14–16].

² Formulas including the $\delta\varphi_{\tilde{g}}$ contributions can be found in Sect. 2.1.2 in Ref. [16].

Ref. [19]. From the $\overline{\text{MS}}$ value the $\overline{\text{DR}}$ value is obtained at the two-loop level (with $n_f = 6$ for $\mu_R > m_t$) via [23]

$$\alpha_s^{\overline{\text{DR}},(6)}(\mu_R) = \alpha_s^{\overline{\text{MS}},(6)}(\mu_R) \left[1 + \frac{\alpha_s^{\overline{\text{MS}},(6)}(\mu_R)}{4\pi} + \frac{7}{8} \frac{(\alpha_s^{\overline{\text{MS}},(6)}(\mu_R))^2}{\pi^2} \right] \quad (29)$$

Within the MSSM α_s to one-loop reads

$$\alpha_s^{\text{MSSM}}(\mu_R) = \alpha_s^{\overline{\text{DR}},(6)}(\mu_R) \left[1 + \frac{\alpha_s^{\overline{\text{DR}},(6)}(\mu_R)}{\pi} \left(\ln \frac{\mu_R}{m_{\tilde{g}}} + \ln \frac{\mu_R}{M_{\tilde{q}}} \right) \right], \quad (30)$$

with $M_{\tilde{q}} = \Pi_{\tilde{q}}(m_{\tilde{q}_1} m_{\tilde{q}_2})^{\frac{1}{12}}$. The log terms origin from the decoupling of the SUSY QCD (SQCD) particles from the running of α_s at lower scales $\mu_R \leq \mu_{\text{dec.}} = m_{\tilde{g}}$.

2.4 The Higgs and gauge boson sector of the cMSSM

The two Higgs doublets of the cMSSM are decomposed in the following way,

$$\begin{aligned} \mathcal{H}_1 &= \begin{pmatrix} H_{11} \\ H_{12} \end{pmatrix} = \begin{pmatrix} v_1 + \frac{1}{\sqrt{2}}(\phi_1 - i\chi_1) \\ -\phi_1^- \end{pmatrix}, \\ \mathcal{H}_2 &= \begin{pmatrix} H_{21} \\ H_{22} \end{pmatrix} = e^{i\xi} \begin{pmatrix} \phi_2^+ \\ v_2 + \frac{1}{\sqrt{2}}(\phi_2 + i\chi_2) \end{pmatrix}. \end{aligned} \quad (31)$$

Besides the vacuum expectation values v_1 and v_2 , in Eq. (31) a possible new phase ξ between the two Higgs doublets is introduced. The Higgs potential V_H can be written in powers of the Higgs fields³,

$$\begin{aligned} V_H &= \dots + T_{\phi_1} \phi_1 + T_{\phi_2} \phi_2 + T_{\chi_1} \chi_1 + T_{\chi_2} \chi_2 \\ &\quad - \frac{1}{2} (\phi_1, \phi_2, \chi_1, \chi_2) \mathbf{M}_{\phi\phi\chi\chi} \begin{pmatrix} \phi_1 \\ \phi_2 \\ \chi_1 \\ \chi_2 \end{pmatrix} - (\phi_1^+, \phi_2^+) \mathbf{M}_{\phi^\pm\phi^\pm}^\top \begin{pmatrix} \phi_1^- \\ \phi_2^- \end{pmatrix} + \dots, \end{aligned} \quad (32)$$

where the coefficients of the linear terms are called tadpoles and those of the bilinear terms are the mass matrices $\mathbf{M}_{\phi\phi\chi\chi}$ and $\mathbf{M}_{\phi^\pm\phi^\pm}$. After a rotation to the physical fields one obtains

$$\begin{aligned} V_H &= \dots + T_h h + T_H H + T_A A \\ &\quad - \frac{1}{2} (h, H, A, G) \mathbf{M}_{hHAG}^{\text{diag}} \begin{pmatrix} h \\ H \\ A \\ G \end{pmatrix} - (H^+, G^+) \mathbf{M}_{H^\pm G^\pm}^{\text{diag}} \begin{pmatrix} H^- \\ G^- \end{pmatrix} + \dots, \end{aligned} \quad (33)$$

³ Corresponding to the convention used in `FeynArts/FormCalc`, we exchanged in the charged part the positive Higgs fields with the negative ones, which is in contrast to Ref. [13]. As we keep the definition of the matrix $\mathbf{M}_{\phi^\pm\phi^\pm}$ used in Ref. [13] the transposed matrix will appear in the expression for $\mathbf{M}_{H^\pm G^\pm}^{\text{diag}}$.

where the tree-level masses are denoted as $m_h, m_H, m_A, m_G, M_{H^\pm}, m_{G^\pm}$. With the help of a Peccei-Quinn transformation [24] μ and the complex soft SUSY-breaking parameters in the Higgs sector can be redefined [25] such that the complex phases vanish at tree-level. As input parameter we choose the mass of the charged Higgs boson, M_{H^\pm} . All details can be found in Refs. [13, 16].

Higgs bosons, h^0, H^0, H^\pm, A^0 , and the electroweak gauge bosons, Z, W^\pm, γ , appear only as internal particles, hence no renormalization is required. Furthermore we use tree-level masses and couplings for the Higgs bosons that appear internally in the loops, see Sect. 3. The only exception is the renormalization of $\tan\beta$ that enters the squark field renormalization. Here we choose a $\overline{\text{DR}}$ scheme as defined, for instance, in Eq. (120c) in Ref. [16].

2.5 The chargino/neutralino sector of the cMSSM

The mass eigenstates of the charginos can be determined from the matrix

$$\mathbf{X} = \begin{pmatrix} M_2 & \sqrt{2} \sin\beta M_W \\ \sqrt{2} \cos\beta M_W & \mu \end{pmatrix}. \quad (34)$$

In addition to the higgsino mass parameter μ it contains the soft breaking term M_2 , which can also be complex in the cMSSM. The rotation to the chargino mass eigenstates is done by transforming the original wino and higgsino fields with the help of two unitary 2×2 matrices \mathbf{U} and \mathbf{V} ,

$$\tilde{\chi}_i^- = \begin{pmatrix} \psi_i^L \\ \psi_i^R \end{pmatrix} \quad \text{with} \quad \psi_i^L = U_{ij} \begin{pmatrix} \tilde{W}^- \\ \tilde{H}_1^- \end{pmatrix}_j \quad \text{and} \quad \psi_i^R = V_{ij} \begin{pmatrix} \tilde{W}^+ \\ \tilde{H}_2^+ \end{pmatrix}_j, \quad (35)$$

where the i th mass eigenstate can be expressed in terms of either the Weyl spinors ψ_i^L and ψ_i^R or the Dirac spinor $\tilde{\chi}_i^-$ with $i, j = 1, 2$.

These rotations lead to the diagonal mass matrix

$$\mathbf{M}_{\tilde{\chi}^-} = \mathbf{V}^* \mathbf{X}^\top \mathbf{U}^\dagger = \begin{pmatrix} m_{\tilde{\chi}_1^\pm} & 0 \\ 0 & m_{\tilde{\chi}_2^\pm} \end{pmatrix}. \quad (36)$$

From this relation, it becomes clear that the chargino masses $m_{\tilde{\chi}_{1,2}^\pm}$ can be determined as the (real and positive) singular values of \mathbf{X} . The singular value decomposition of \mathbf{X} also yields results for \mathbf{U} and \mathbf{V} .

A similar procedure is used for the determination of the neutralino masses and mixing matrix, which can both be calculated from the mass matrix

$$\mathbf{Y} = \begin{pmatrix} M_1 & 0 & -M_Z s_w \cos\beta & M_Z s_w \sin\beta \\ 0 & M_2 & M_Z c_w \cos\beta & -M_Z c_w \sin\beta \\ -M_Z s_w \cos\beta & M_Z c_w \cos\beta & 0 & -\mu \\ M_Z s_w \sin\beta & -M_Z c_w \sin\beta & -\mu & 0 \end{pmatrix}. \quad (37)$$

This symmetric matrix contains the additional complex soft-breaking parameter M_1 . The diagonalization of the matrix is achieved by a transformation starting from the original bino/wino/higgsino basis,

$$\tilde{\chi}_k^0 = \begin{pmatrix} \psi_k^0 \\ \psi_k^0 \end{pmatrix}, \quad \psi_k^0 = N_{kl} \begin{pmatrix} \tilde{B}^0 \\ \tilde{W}^0 \\ \tilde{H}_1^0 \\ \tilde{H}_2^0 \end{pmatrix}_l, \quad \mathbf{M}_{\tilde{\chi}^0} = \mathbf{N}^* \mathbf{Y} \mathbf{N}^\dagger = \begin{pmatrix} m_{\tilde{\chi}_1^0} & 0 & 0 & 0 \\ 0 & m_{\tilde{\chi}_2^0} & 0 & 0 \\ 0 & 0 & m_{\tilde{\chi}_3^0} & 0 \\ 0 & 0 & 0 & m_{\tilde{\chi}_4^0} \end{pmatrix}, \quad (38)$$

where ψ_k^0 denotes the two component Weyl spinor and $\tilde{\chi}_k^0$ the four component Majorana spinor of the k th neutralino field with $k, l = 1, 2, 3, 4$. The unitary 4×4 matrix \mathbf{N} and the physical neutralino masses again result from a numerical singular value decomposition of \mathbf{Y} . The symmetry of \mathbf{Y} permits the non-trivial condition of using only one matrix \mathbf{N} for its diagonalization, in contrast to the chargino case shown above.

A renormalization of this sector, as described in detail in Refs. [14, 16], is not required. Neutralinos and charginos appear only as internal particles in the loop corrections of the two-body decays, see Sect. 3. In addition, neutralinos appear as external particles only in purely loop-induced processes, see Eqs. (1) – (3). Consequently, we obtained our results by using tree-level masses and couplings in the chargino and neutralino sector. Again, the only exception is the renormalization of μ entering the squark field renormalization. We follow the on-shell prescription given in Ref. [16], where $\delta\mu$ is defined in Eq. (181).

3 Calculation of loop diagrams

In this section we give some details about the calculation of the higher-order corrections to the gluino decays. Sample diagrams are shown in Figs. 1, 2. Not shown are the diagrams for real (hard and soft) photon and gluon radiation. They are included via analytical formulas following the description given in Ref. [18].

The internal generically depicted particles in Figs. 1, 2 are labeled as follows: F can be a quark, chargino, neutralino or \tilde{g} , S can be a squark or a Higgs boson, V can be a γ , Z , W^\pm or g . Internally appearing Higgs bosons do not receive higher-order corrections in their masses or couplings, which would correspond to effects beyond one-loop.⁴

In Fig. 1 we have furthermore omitted in general diagrams of self-energy type of external (on-shell) particles. While the real part of such a loop does not contribute to the decay width due to the on-shell renormalization, the imaginary part, in product with an imaginary part of a complex coupling (in our case coming from $\varphi_{\tilde{g}}$) can give a real contribution to the decay width. While these diagrams are not shown explicitly, they have been taken into account in the analytical and numerical evaluation via renormalization constants, see Sect. 2. The impact of those absorptive contributions will be discussed in Sect. 4.3.

The diagrams and corresponding amplitudes have been obtained with **FeynArts** [26]. The model file, including the MSSM counter terms, is based on Ref. [14–16], i.e. to match exactly the renormalization prescription described in those articles (see also Ref. [27] for other sectors). The further evaluation has been performed with **FormCalc** (and **LoopTools**) [28]. As

⁴ We found that using loop corrected Higgs boson masses for the internal Higgs bosons also result in finite results, where the numerical difference for the various decay widths is negligible.

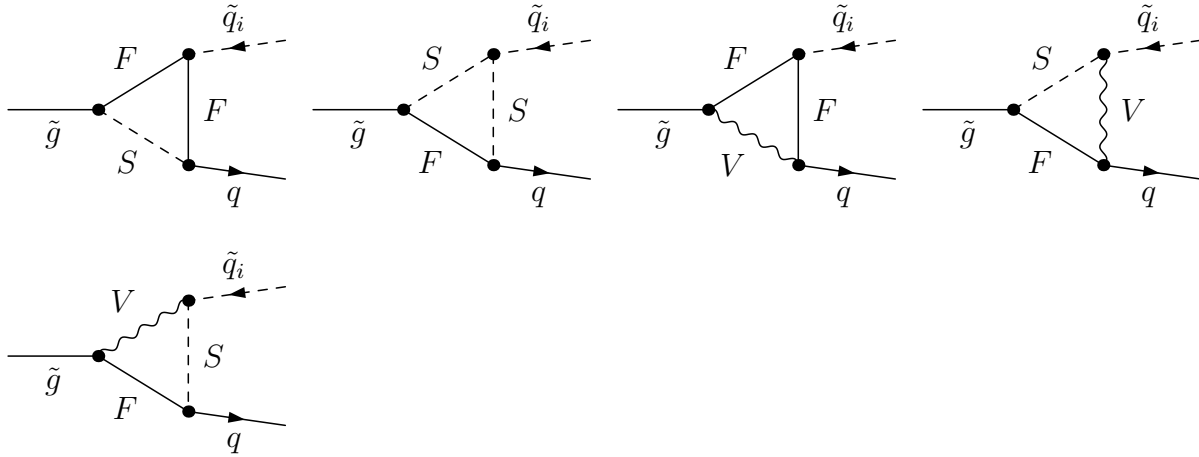


Figure 1: Generic Feynman diagrams for the decay $\tilde{g} \rightarrow \tilde{q}_i q$ ($i = 1, 2$). F can be a quark, chargino, neutralino or \tilde{g} , S can be a squark or a Higgs boson, V can be a γ , Z , W^\pm or g . The tree-level diagram is not shown here.

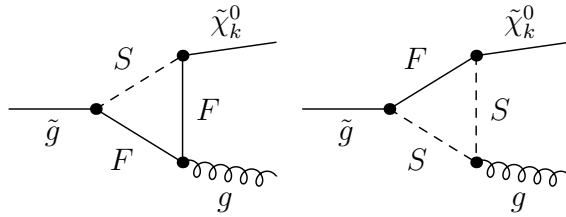


Figure 2: Generic Feynman diagrams for the decay $\tilde{g} \rightarrow \tilde{\chi}_k^0 g$ ($k = 1, 2, 3, 4$). Here F denotes a quark and S a squark. It should be noted that this process exists only at the loop-level.

regularization scheme for the UV-divergences we have used constrained differential renormalization [29], which has been shown to be equivalent to dimensional reduction [30] at the one-loop level [28]. Thus the employed regularization preserves SUSY [31, 32]. All UV-divergences cancel in the final result.

The IR-divergences from diagrams with an internal photon or gluon have to cancel with the ones from the corresponding real soft radiation. In the case of QED we have included the soft and hard photon contribution following the description given in Ref. [18]. In the case of QCD we have modified this prescription by replacing the product of electric charges by the appropriate combination of color charges (linear combination of C_A and C_F times α_s). The IR-divergences arising from the diagrams involving a γ or a g are regularized by introducing a finite photon mass, or gluon mass, λ . While for the QED part this procedure always works, in the QCD part due to its non-abelian character this method can fail. However, since no triple or quartic gluon vertices appear, λ can indeed be used as a regulator. All IR-divergences, i.e. all divergences in the limit $\lambda \rightarrow 0$, cancel once virtual and real radiation for one decay channel are added.⁵

⁵ Using tree-level, as well as one-loop down-type squark masses (see Sect. 2.1), yields a cancellation of IR divergences to all orders for all \tilde{g} decays.

For completeness we show here also the formulas for the tree-level decay widths:

$$\Gamma^{\text{tree}}(\tilde{g} \rightarrow \tilde{q}_i q) = \left[(|C(\tilde{g}, \tilde{q}_i, q)_L|^2 + |C(\tilde{g}, \tilde{q}_i, q)_R|^2) (m_{\tilde{g}}^2 - m_{\tilde{q}_i}^2 + m_q^2) + 4 \operatorname{Re}\{C(\tilde{g}, \tilde{q}_i, q)_L^* C(\tilde{g}, \tilde{q}_i, q)_R\} m_{\tilde{g}} m_q \right] \frac{\lambda^{1/2}(m_{\tilde{g}}^2, m_{\tilde{q}_i}^2, m_q^2)}{64 \pi m_{\tilde{g}}^3}, \quad (39)$$

where $\lambda(x, y, z) = (x - y - z)^2 - 4yz$ and the couplings $C(a, b, c)$ can be found in the `FeynArts` model files [33]. $C(a, b, c)_{L,R}$ denote the part of the coupling which is proportional to $\frac{1}{2}(\mathbb{1} \mp \gamma_5)$.

4 Numerical analysis

In this section we present a numerical analysis of all 28 decay channels (“xy”). In the various figures we show the decay width and its relative correction at the tree-level (“tree”) and at the one-loop level (“full”),

$$\Gamma^{\text{tree}} \equiv \Gamma^{\text{tree}}(\tilde{g} \rightarrow xy), \quad \Gamma^{\text{full}} \equiv \Gamma^{\text{full}}(\tilde{g} \rightarrow xy), \quad \delta\Gamma/\Gamma^{\text{tree}} \equiv \frac{\Gamma^{\text{full}} - \Gamma^{\text{tree}}}{\Gamma^{\text{tree}}}. \quad (40)$$

The total decay width is defined as the sum of the 24 decay widths⁶,

$$\Gamma_{\text{tot}}^{\text{tree}} \equiv \sum_{xy} \Gamma^{\text{tree}}(\tilde{g} \rightarrow xy), \quad \Gamma_{\text{tot}}^{\text{full}} \equiv \sum_{xy} \Gamma^{\text{full}}(\tilde{g} \rightarrow xy), \quad \delta\Gamma_{\text{tot}}/\Gamma_{\text{tot}}^{\text{tree}} \equiv \frac{\Gamma_{\text{tot}}^{\text{full}} - \Gamma_{\text{tot}}^{\text{tree}}}{\Gamma_{\text{tot}}^{\text{tree}}}. \quad (41)$$

We also show the absolute and relative changes of the branching ratios,

$$\text{BR}^{\text{tree}} \equiv \frac{\Gamma^{\text{tree}}(\tilde{g} \rightarrow xy)}{\Gamma_{\text{tot}}^{\text{tree}}}, \quad \text{BR}^{\text{full}} \equiv \frac{\Gamma^{\text{full}}(\tilde{g} \rightarrow xy)}{\Gamma_{\text{tot}}^{\text{full}}}, \quad \delta\text{BR}/\text{BR} \equiv \frac{\text{BR}^{\text{full}} - \text{BR}^{\text{tree}}}{\text{BR}^{\text{full}}}. \quad (42)$$

The last quantity is crucial to analyze the impact of the one-loop corrections on the phenomenology at the LHC.

4.1 Parameter settings

The renormalization scale, μ_R , has been set to the mass of the decaying particle, i.e. $\mu_R = m_{\tilde{g}}$. The SM parameters are chosen as follows, see also [19]:

- Fermion masses:

$$\begin{aligned} m_e &= 0.51099891 \text{ MeV}, & m_{\nu_e} &= 0 \text{ MeV}, \\ m_\mu &= 105.658367 \text{ MeV}, & m_{\nu_\mu} &= 0 \text{ MeV}, \\ m_\tau &= 1776.82 \text{ MeV}, & m_{\nu_\tau} &= 0 \text{ MeV}, \\ m_u &= 53.8 \text{ MeV}, & m_d &= 53.8 \text{ MeV}, \end{aligned}$$

⁶ We neglected the $\tilde{g} \rightarrow \tilde{\chi}_k^0 g$ decays in the total decay width due to their negligible contribution, see Sect. 4.4 and Sect. 4.5.

$$\begin{aligned}
m_c &= 1.27 \text{ GeV} , & m_s &= 101 \text{ MeV} , \\
m_t &= 172.0 \text{ GeV} , & m_b^{\overline{\text{MS}}}(m_b) &= 4.25 \text{ GeV} .
\end{aligned}
\tag{43}$$

m_u and m_d are effective parameters, calculated through the hadronic contributions to:

$$\Delta\alpha_{\text{had}}^{(5)}(M_Z) = \frac{\alpha}{\pi} \sum_{f=u,c,d,s,b} Q_f^2 \left(\ln \frac{M_Z^2}{m_f^2} - \frac{5}{3} \right) .
\tag{44}$$

- The CKM matrix has been set to unity.
- Gauge boson masses:

$$M_Z = 91.1876 \text{ GeV} , \quad M_W = 80.399 \text{ GeV} ,
\tag{45}$$

- Coupling constants:

$$\alpha = 1/137.035999679 , \quad \alpha_s^{\overline{\text{MS}}}(M_Z) = 0.1184 .
\tag{46}$$

The Higgs sector quantities (masses, etc. at the tree-level) have been evaluated using the `FormCalc` implementation [28].

We will show the results for one representative numerical example. The parameters are chosen according to the scenario \mathcal{S} shown in Tab. 1, but with one of the parameters varied. The scenarios are defined such that *all* decay modes are open simultaneously to permit an analysis of all channels, i.e. not picking specific parameters for each decay. We will start with a variation of $m_{\tilde{g}}$, and show later the results for varying $\varphi_{\tilde{g}}$. The scenarios are in agreement with the MSSM Higgs boson searches at LEP [34, 35]. The choice of relatively large gluino and squark masses also avoids all LHC bounds [36]. The slepton/lepton sector of the cMSSM does not enter into our calculation, hence the parameters are not specified. Furthermore, also the following exclusion limits [19] hold in our scenario:

$$m_{\tilde{\chi}_1^0} > 46 \text{ GeV}, \quad m_{\tilde{\chi}_2^0} > 62 \text{ GeV}, \quad m_{\tilde{\chi}_3^0} > 100 \text{ GeV}, \quad m_{\tilde{\chi}_4^0} > 116 \text{ GeV}, \quad m_{\tilde{\chi}_1^\pm} > 94 \text{ GeV} .
\tag{47}$$

The scalar quark masses of the parameter set \mathcal{S} are shown in Tab. 2. The values of $m_{\tilde{g}}$ allow copious production of the gluino at the LHC, once $\sqrt{s} = 14 \text{ TeV}$ is reached.

The numerical results we will show in the next subsections are of course dependent on choice of the SUSY parameters. Nevertheless, they give an idea of the relevance of the full one-loop corrections. As an example, the various decay widths $\Gamma(\tilde{g} \rightarrow \tilde{q}_i q)$ are all of similar size, contributing similarly to Γ_{tot} . The same holds for the various branching ratios. If the (artificial) degeneracy of the soft SUSY-breaking parameters in the squark sector were lifted, these results could change significantly. However, the size of the loop corrections shown in our numerical example still gives a good indication about the size of the expected corrections. In the special case of $m_{\tilde{g}} < m_{\tilde{q}_i}$ (for all \tilde{q} and $i = 1, 2$) the loop-induced decays $\tilde{g} \rightarrow \tilde{\chi}_k^0 g$ ($k = 1, 2, 3, 4$) as well as three-body decays (which are not investigated here) could become dominant.

Scen.	$\tan \beta$	M_{H^\pm}	$M_{\tilde{q}_L}$	$M_{\tilde{q}_R}$	μ	A_t	A_b	M_1	M_2	M_3
\mathcal{S}	20	200	700	800	200	1000	800	200	300	1200

Table 1: MSSM parameters for the initial numerical investigation; all masses are in GeV. For the \tilde{q} sector the shifts in $M_{\tilde{q}_{L,R}}$ as defined in Eqs. (49) and (50) in Ref. [16] are taken into account. The values for $A_t (= A_c = A_u)$ and $A_b (= A_s = A_d)$ are chosen such that charge- or color-breaking minima are avoided [37].

\tilde{q} -type	\tilde{u}	\tilde{c}	\tilde{t}	\tilde{d}	\tilde{s}	\tilde{b}
$m_{\tilde{q}_1}$	697.919	697.913	637.268	702.402	702.402	705.879
$m_{\tilde{q}_2}$	799.232	799.240	882.565	800.384	800.384	800.848

Table 2: The scalar quark masses in \mathcal{S} for the numerical investigation; all masses are in GeV and rounded to one MeV.

4.2 Full one-loop results for varying $m_{\tilde{g}}$

The results shown in this and the following subsections consist of “tree”, which denotes the tree-level value and of “full”, which is the decay width including *all* one-loop corrections as described in Sect. 3. Additionally in this section we also investigate the accuracy of the pure SUSY QCD corrections for the decay widths as evaluated for real parameters in Ref. [5].⁷ The corresponding curves are labelled “SQCD”. We start the numerical analysis with \tilde{g} decay widths evaluated as a function of $m_{\tilde{g}}$ starting at $m_{\tilde{g}} = 700$ GeV up to $m_{\tilde{g}} = 2$ TeV, which roughly coincides with the reach of the LHC for high-luminosity running. The upper panels contain the results for the absolute value of the various decay widths, $\Gamma(\tilde{g} \rightarrow xy)$ (left) and the relative correction from the full one-loop contributions (right), where we compare “tree”, “full” and “SQCD”. The lower panels show the same results (but leaving out “SQCD”) for $\text{BR}(\tilde{g} \rightarrow xy)$.

Since all parameters are chosen real no difference between the two decay modes $\tilde{g} \rightarrow \tilde{q}_i^\dagger q$ and $\tilde{g} \rightarrow \tilde{q}_i \bar{q}$ arises, neither in the decay widths, nor in the branching ratios (where of course both channels are taken into account in the total decay width). Consequently, we only show results for the channel “ $\tilde{g} \rightarrow \tilde{q}_i q$ ”, and the results for $\text{BR}(\tilde{g} \rightarrow \tilde{q}_i^\dagger q + \tilde{g} \rightarrow \tilde{q}_i \bar{q})$ are simply the $\text{BR}(\tilde{g} \rightarrow \tilde{q}_i q)$ multiplied by two. In Sect. 4.3 both channels will be shown separately. Furthermore, due to the absence of complex parameters no contributions from absorptive parts of self-energy type corrections on external legs can contribute. Again, this will be different in Sect. 4.3.

In our numerical scenario \mathcal{S} we have chosen a small splitting between the left- and the right-handed soft SUSY-breaking parameter within all squark flavors, see Tab. 1. If the effects of mass differences of the quark and squarks in the final state were neglected one

⁷ We have checked that we are in good agreement with Ref. [5] using their input parameters, where a small difference remains due to the different renormalization schemes.

would expect $\sum_{i=1,2} \text{BR}(\tilde{g} \rightarrow \tilde{q}_i q) \approx 1/12$ (or $\sum_{i=1,2} \text{BR}(\tilde{g} \rightarrow \tilde{q}_i^\dagger q + \tilde{g} \rightarrow \tilde{q}_i \bar{q}) \approx 1/6$ if both combinations are taken into account). Deviations from this number are expected due to kinematical effects, and differences in the loop corrections (including possible effects related to the scalar quark mixing). For large values of $m_{\tilde{g}}$ where mass effects should be small it is expected to reach the value of $\sim 1/12$.

We start with the decay $\tilde{g} \rightarrow \tilde{t}_1 t$. The results for this channel are shown in Fig. 3 as a function of $m_{\tilde{g}}$. The tiny dip in \mathcal{S} at $m_{\tilde{g}} \approx 1054.6$ GeV is the threshold $m_{\tilde{g}} = m_{\tilde{t}_2} + m_t$ of the self energy $\Sigma_{\tilde{g}}(m_{\tilde{g}}^2)$ in the renormalization constants $\delta Z_{\tilde{g}}$ and δM_3 . One can see that the size of the corrections of the decay width is especially large very close to the production threshold.⁸ Away from the production threshold relative corrections of $\sim -6\%$ are found. The difference between the full and the SQCD corrections is roughly 5%; at low masses the EW corrections are about one third of the full corrections, while at large $m_{\tilde{g}}$ they are dominating over the SQCD corrections. The branching ratio in our numerical scenario \mathcal{S} (where we have scalar quarks very close in mass) can reach more than 12% close to threshold and stays above 5% for large $m_{\tilde{g}}$. The correction to the branching ratio is then found to be $\sim -4\%$.

Next, in Fig. 4 we show the decay $\Gamma(\tilde{g} \rightarrow \tilde{t}_2 t)$. At low $m_{\tilde{g}}$ the decay is kinematically forbidden and reaches ~ 11 GeV at $m_{\tilde{g}} = 2$ TeV, with small positive corrections to the decay width at low $m_{\tilde{g}}$ and very small negative corrections at large $m_{\tilde{g}}$. The behavior of the SQCD corrections alone is quite different for this decay. They are large and negative, $\sim -14\%$ close to threshold and turn positive up to $+2\%$ for large $m_{\tilde{g}}$. The SQCD contributions alone constitute a very weak approximation to the full result in this channel. The BR reaches nearly 3% at large $m_{\tilde{g}}$, so that $\text{BR}(\tilde{g} \rightarrow \tilde{t}_1 t) + \text{BR}(\tilde{g} \rightarrow \tilde{t}_2 t) \approx 8.5\% \sim 1/12$ is reached. The relative corrections reach from 10% where the width is small going down below 1% where the width and BR are largest.

Now we turn to the decays to \tilde{b}/b . The results for the decay $\tilde{g} \rightarrow \tilde{b}_1 b$ are presented in Fig. 5. Within \mathcal{S} the first dip at $m_{\tilde{g}} \approx 800.51$ GeV stems from the threshold $m_{\tilde{g}} = m_{\tilde{c}_2} + m_c$ in the self energy $\Sigma_{\tilde{g}}(m_{\tilde{g}}^2)$ entering the renormalization constants $\delta Z_{\tilde{g}}$ and δM_3 . The second dip at $m_{\tilde{g}} \approx 1054.6$ GeV comes from the threshold $m_{\tilde{g}} = m_{\tilde{t}_2} + m_t$. As expected the decay width rises from zero at threshold to ~ 15.5 GeV at $m_{\tilde{g}} = 2$ TeV, including the full one-loop corrections. The first threshold leads to very large corrections of nearly -14% , which then decreases to $\sim -5\%$ at larger $m_{\tilde{g}}$ values. The SQCD corrections approximate the full result quite well up to $m_{\tilde{g}} = 1200$ GeV, but then tend to zero. Again for large $m_{\tilde{g}}$ the full corrections are dominated by the EW contributions. The first threshold is also clearly visible in the BR, where values around 9% can be reached, going down to $\sim 4\%$ at $m_{\tilde{g}} = 2$ TeV. The relative corrections to the BR vary between -4% and $+0.5\%$ around the first threshold and go to -3% at high $m_{\tilde{g}}$ values.

The results for $\tilde{g} \rightarrow \tilde{b}_2 b$ are shown in Fig. 6. Again the dip at $m_{\tilde{g}} \approx 1054.6$ GeV comes from the threshold $m_{\tilde{g}} = m_{\tilde{t}_2} + m_t$. The threshold $m_{\tilde{g}} = m_{\tilde{c}_2} + m_c$ and the corresponding large effects observed for $\tilde{g} \rightarrow \tilde{b}_1 b$ are absent here due to the fact that $m_{\tilde{b}_2} = 800.848$ GeV. Apart from this we find for the decay widths the expected values with $\Gamma(\tilde{g} \rightarrow \tilde{b}_2 b) \sim 15$ GeV at

⁸ It should be noted that a calculation very close to threshold requires the inclusion of additional (non-relativistic) contributions, which is beyond the scope of this paper. Consequently, very close to threshold our calculation (at the tree- or loop-level) does not provide a very accurate description of the decay width.

$m_{\tilde{g}} = 2$ TeV (with the SQCD corrections giving a very good approximation to the full result) and a corresponding BR of $\sim 4\%$. Again the sum of the two BR's reaches $\sim 8.5\% \sim 1/12$. The relative corrections can reach nearly -9% at $m_{\tilde{g}} \approx 900$ GeV for the decay width and values between $+9\%$ and $+2\%$ for small and large BR's, respectively.

Next we analyze the effects in the decays involving second generation (s)quarks. We start with the decay $\tilde{g} \rightarrow \tilde{c}_1 c$ shown in Fig. 7. Two dips are visible: within \mathcal{S} the first dip appears at $m_{\tilde{g}} \approx 809.3$ GeV, due to the threshold $m_{\tilde{g}} = m_{\tilde{t}_1} + m_t$. The second dip at $m_{\tilde{g}} \approx 1054.6$ GeV comes from the threshold $m_{\tilde{g}} = m_{\tilde{t}_2} + m_t$. The decay width behaves “as expected”, rising up to ~ 16 GeV at $m_{\tilde{g}} = 2$ TeV. The relative corrections are again largest around the first threshold, reaching nearly -10% , flattening out to $\sim -3\%$ at larger $m_{\tilde{g}}$ values. The SQCD corrections alone yield larger corrections by $\sim -5\%$, going to zero for large $m_{\tilde{g}}$, where the EW contributions are dominating. The branching ratio is very large at threshold due to the relative smallness of $m_{\tilde{c}_1} + m_c$ in \mathcal{S} , exceeding 20% . At large $m_{\tilde{g}}$ the “expected” $\sim 4\%$ are reached. The relative correction to the BR exhibits a maximum around $m_{\tilde{g}} = 800$ GeV due to $m_{\tilde{g}} = m_{\tilde{t}_1} + m_t$, see above. At large $m_{\tilde{g}}$ the corrections become very small, but potentially reach larger negative values at $m_{\tilde{g}} > 2$ TeV.

The results for $\tilde{g} \rightarrow \tilde{c}_2 c$ are shown in Fig. 8. Again, the dip at $m_{\tilde{g}} \approx 1054.6$ GeV stems from the threshold $m_{\tilde{g}} = m_{\tilde{t}_2} + m_t$. Decay width and branching ratio show the expected behavior. The BR reaches $\sim 4\%$ at large $m_{\tilde{g}}$, so that the sum of the four “charm BR's” goes to $\sim 1/6$. The corrections to the width are maximal with $\sim -7.5\%$ around $m_{\tilde{g}} = 900$ GeV and rise to small positive values for large $m_{\tilde{g}}$, with the SQCD corrections deviating from this by up to -1% at most. Concerning the branching ratio the effects are largest where the BR is small and reach the level of $\sim 3\%$ at $m_{\tilde{g}} = 2$ TeV.

The decays involving scalar strange quarks, $\tilde{g} \rightarrow \tilde{s}_i s$ ($i = 1, 2$), are shown in Figs. 9, 10. Again several dips are visible, the first dip at $m_{\tilde{g}} \approx 809.3$ GeV comes from the threshold $m_{\tilde{g}} = m_{\tilde{t}_1} + m_t$. Once more the second dip at $m_{\tilde{g}} \approx 1054.6$ GeV is the threshold $m_{\tilde{g}} = m_{\tilde{t}_2} + m_t$. The results are very similar to the ones for the decays $\tilde{g} \rightarrow \tilde{c}_i c$, where differences can only be observed close to threshold due to slightly different masses of the scalar quarks. The most prominent example in this respect is the BR($\tilde{g} \rightarrow \tilde{s}_1 s$) that reaches “only” about 10% for $m_{\tilde{g}} = 700 \dots 800$ GeV. Otherwise the “expected” behavior is found at the tree and at the loop level, including also the size of the pure SQCD corrections.

The results for decays involving first generation (s)quarks are very similar to the ones for the second generation, again differences appear only due to small deviations in the scalar quark masses, see Tab. 2. Otherwise again the “expected” behavior is found with loop corrections yielding maximum values of -10% for the decay widths, again with the same size of the SQCD corrections, and $+5\%$ for the branching ratios. It should be kept in mind that the results found for the branching ratios are highly model dependent, and much larger/smaller values can be found for different kinematical situations.

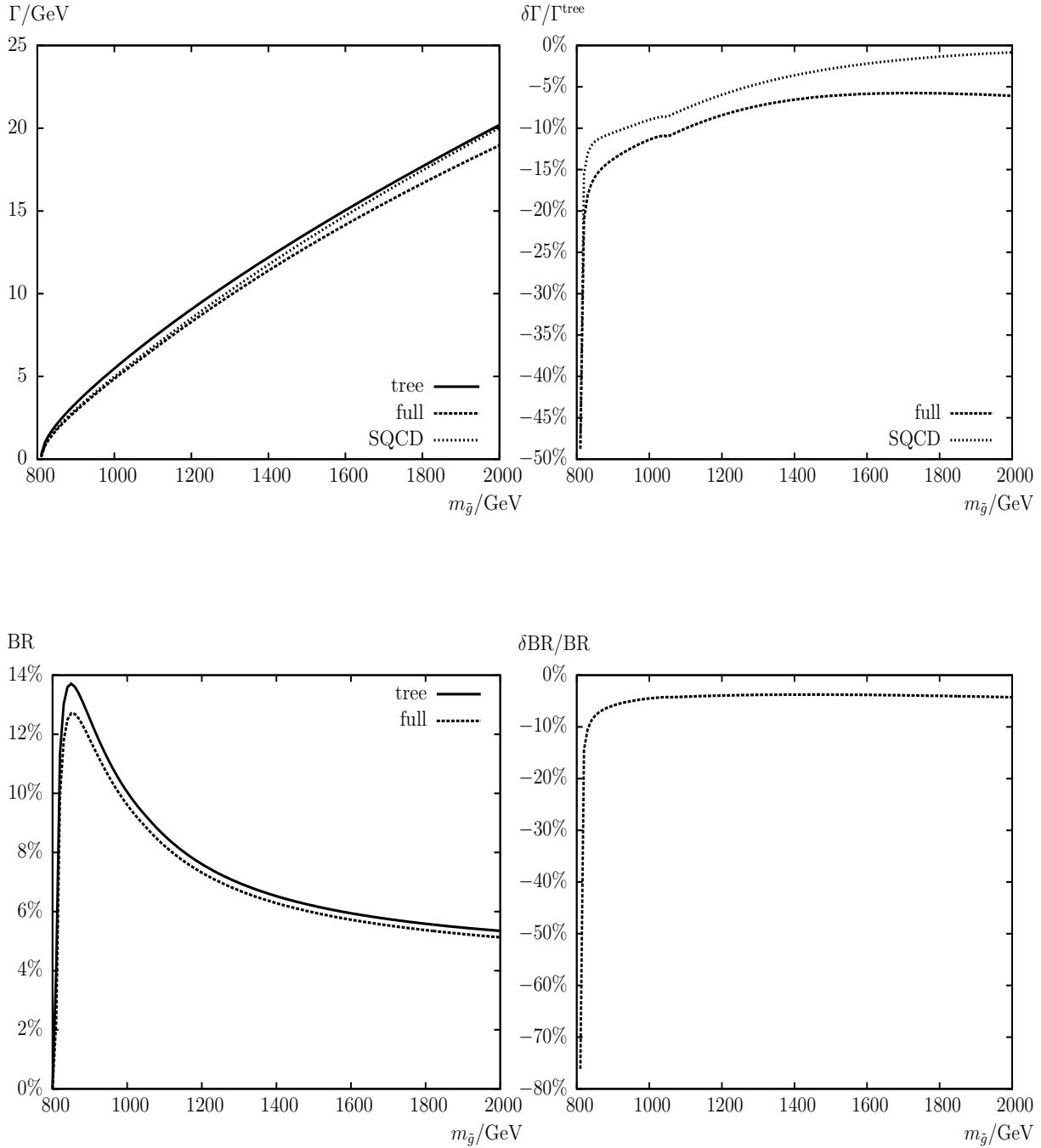


Figure 3: $\Gamma(\tilde{g} \rightarrow \tilde{t}_1 t)$. Tree-level (“tree”) and full one-loop (“full”) corrected decay widths are shown with the parameters chosen according to \mathcal{S} (see Tab. 1), with $m_{\tilde{g}}$ varied. The upper left plot shows the decay width, the upper right plot shows the relative size of the corrections. Also shown are the pure SQCD corrections (“SQCD”). The lower left plot shows the BR, the lower right plot shows the relative size of the BR.

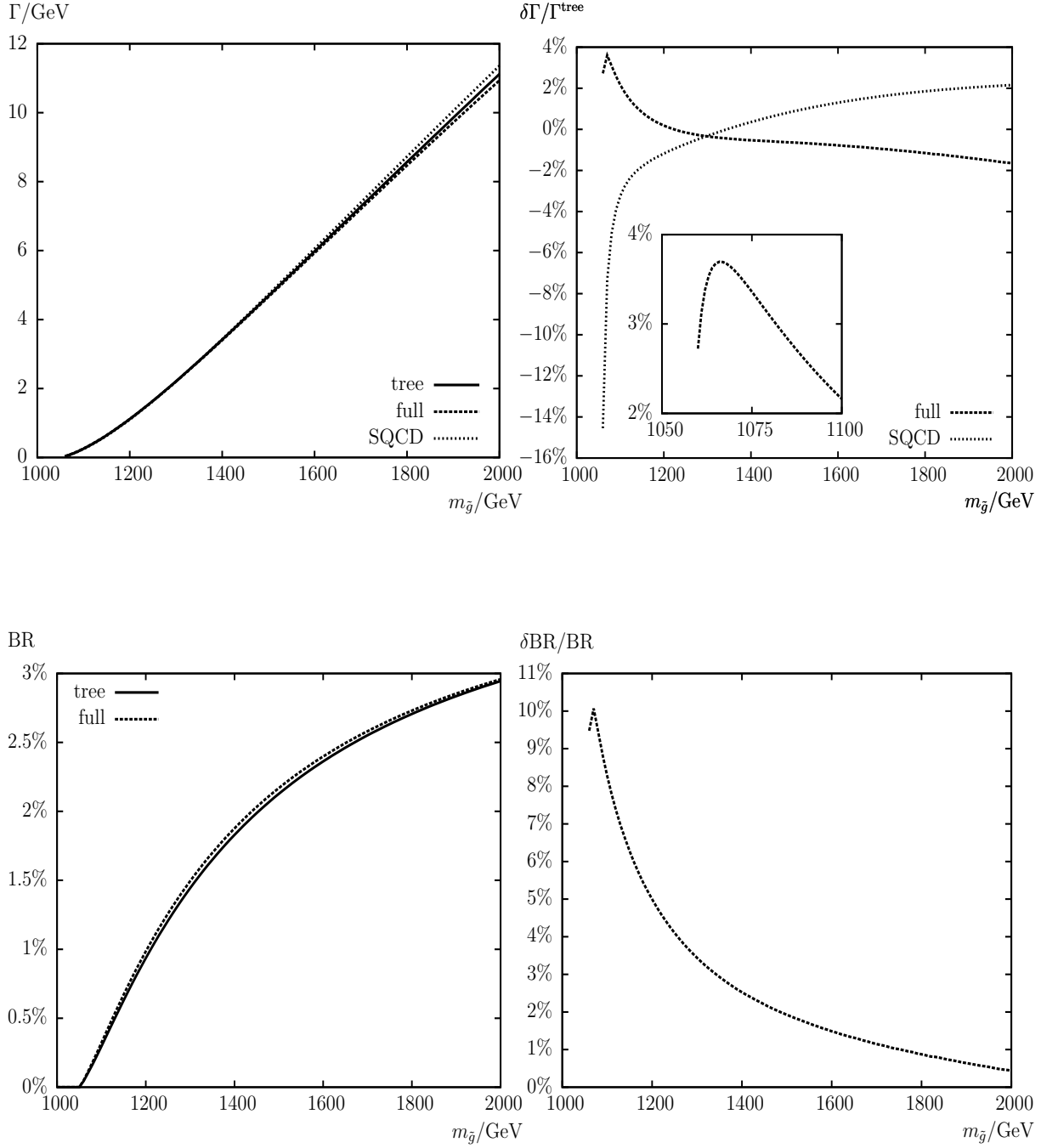


Figure 4: $\Gamma(\tilde{g} \rightarrow \tilde{t}_2 t)$. Tree-level (“tree”) and full one-loop (“full”) corrected decay widths are shown with the parameters chosen according to \mathcal{S} (see Tab. 1), with $m_{\tilde{g}}$ varied. The upper left plot shows the decay width, the upper right plot shows the relative size of the corrections. Also shown are the pure SQCD corrections (“SQCD”). The lower left plot shows the BR, the lower right plot shows the relative size of the BR.

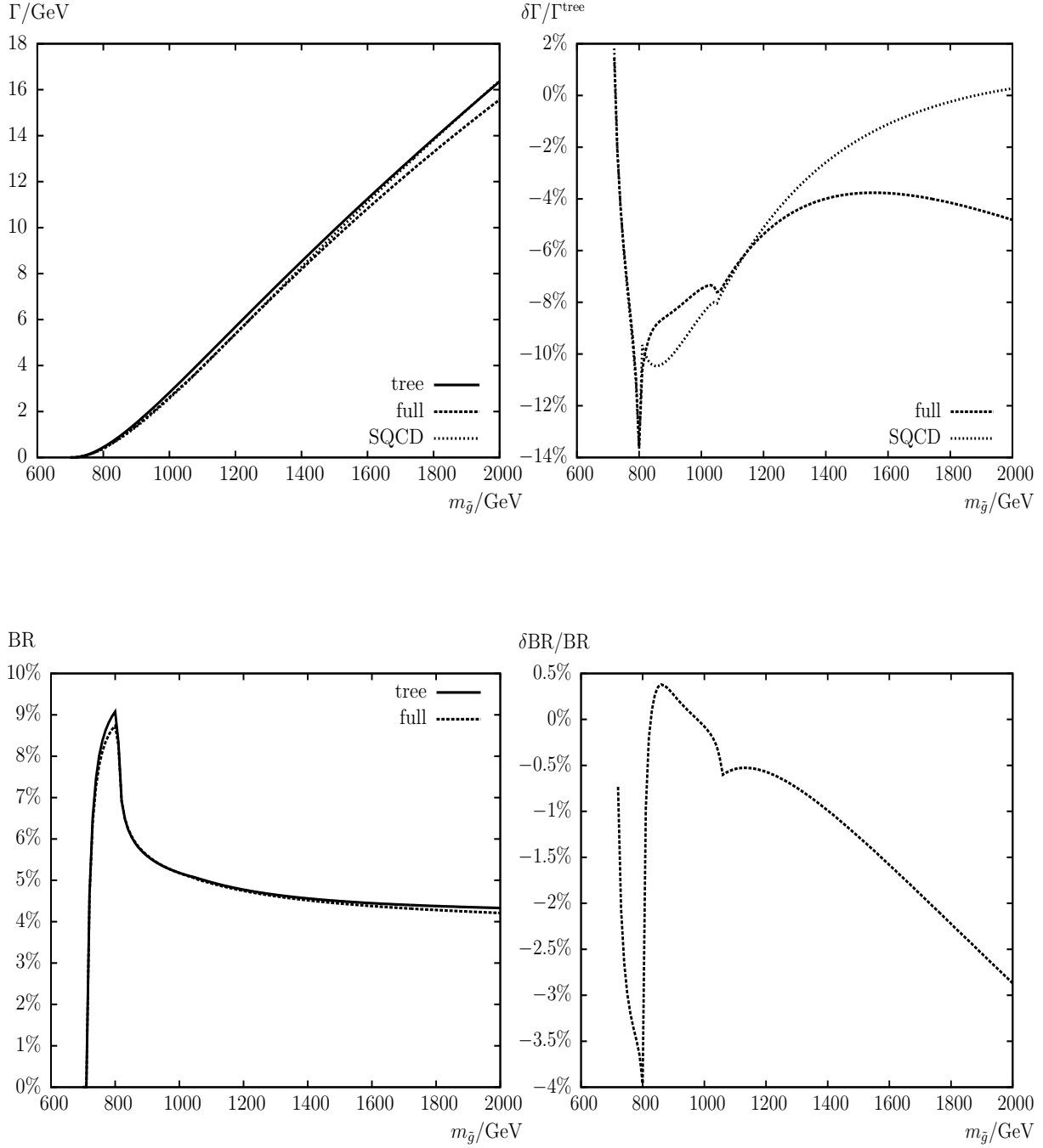


Figure 5: $\Gamma(\tilde{g} \rightarrow \tilde{b}_1 b)$. Tree-level (“tree”) and full one-loop (“full”) corrected decay widths are shown with the parameters chosen according to \mathcal{S} (see Tab. 1), with $m_{\tilde{g}}$ varied. The upper left plot shows the decay width, the upper right plot shows the relative size of the corrections. Also shown are the pure SQCD corrections (“SQCD”). The lower left plot shows the BR, the lower right plot shows the relative size of the BR.

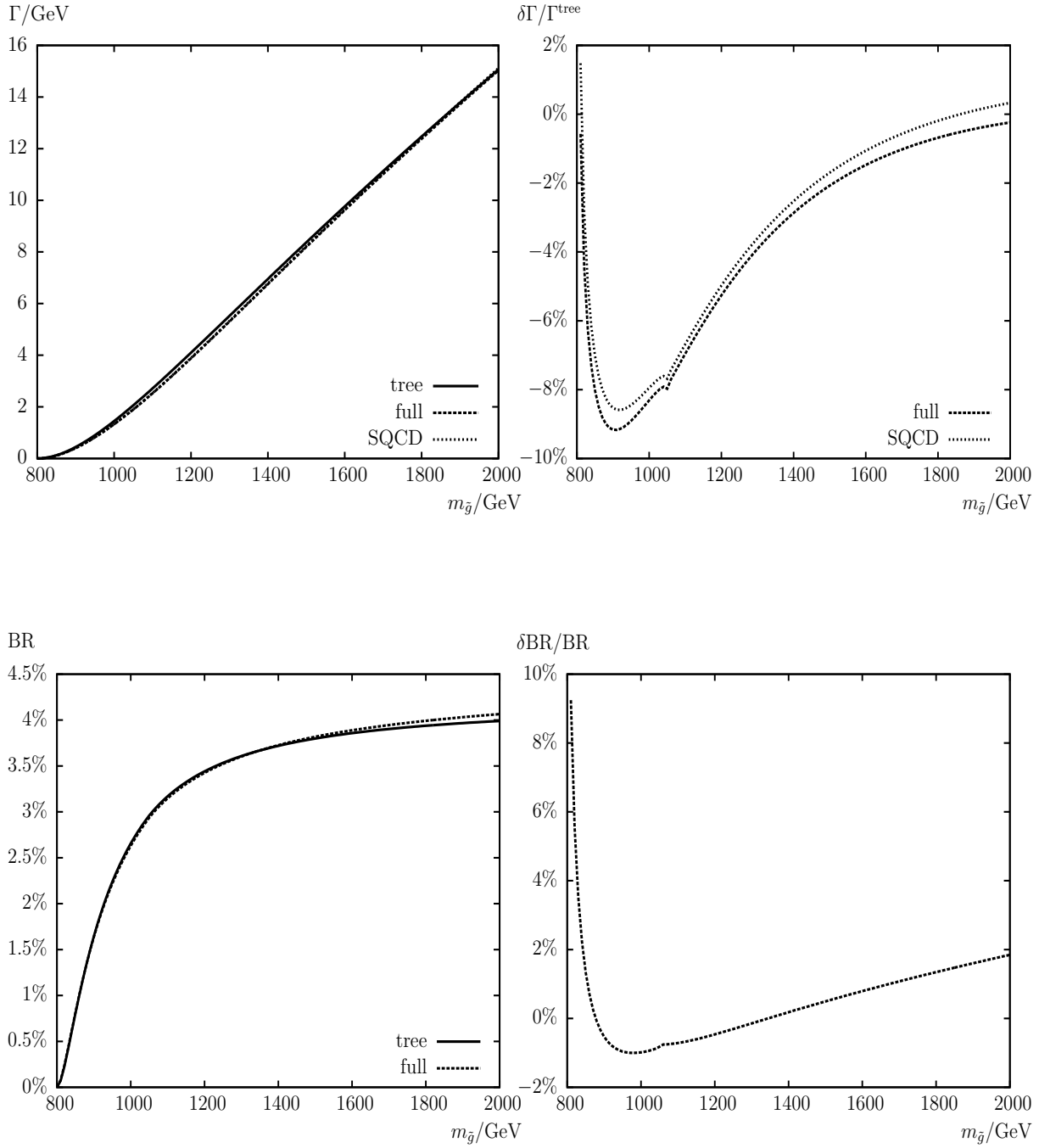


Figure 6: $\Gamma(\tilde{g} \rightarrow \tilde{b}_2 b)$. Tree-level (“tree”) and full one-loop (“full”) corrected decay widths are shown with the parameters chosen according to \mathcal{S} (see Tab. 1), with $m_{\tilde{g}}$ varied. The upper left plot shows the decay width, the upper right plot shows the relative size of the corrections. Also shown are the pure SQCD corrections (“SQCD”). The lower left plot shows the BR, the lower right plot shows the relative size of the BR.

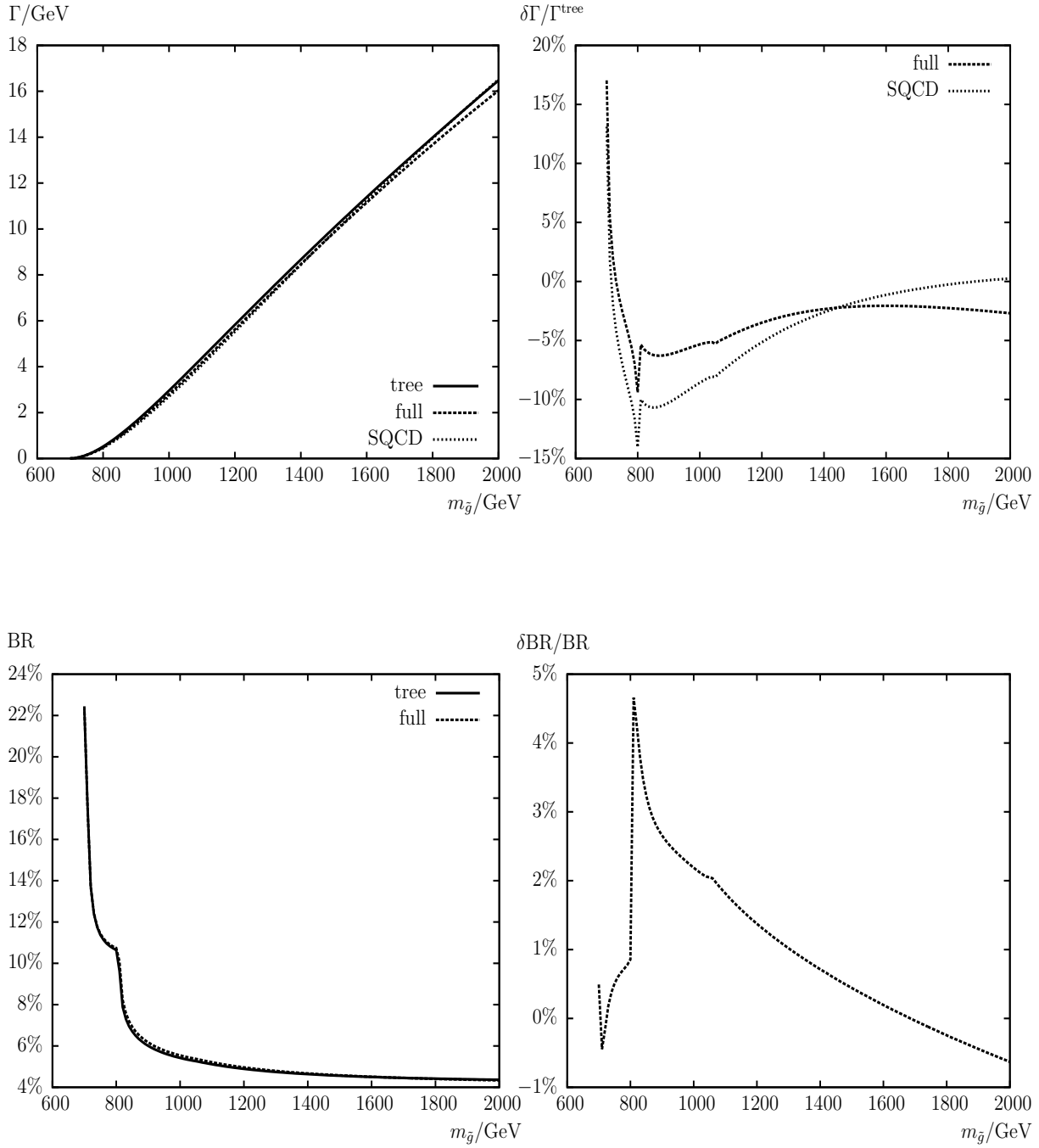


Figure 7: $\Gamma(\tilde{g} \rightarrow \tilde{c}_1 c)$. Tree-level (“tree”) and full one-loop (“full”) corrected decay widths are shown with the parameters chosen according to \mathcal{S} (see Tab. 1), with $m_{\tilde{g}}$ varied. The upper left plot shows the decay width, the upper right plot shows the relative size of the corrections. Also shown are the pure SQCD corrections (“SQCD”). The lower left plot shows the BR, the lower right plot shows the relative size of the BR.

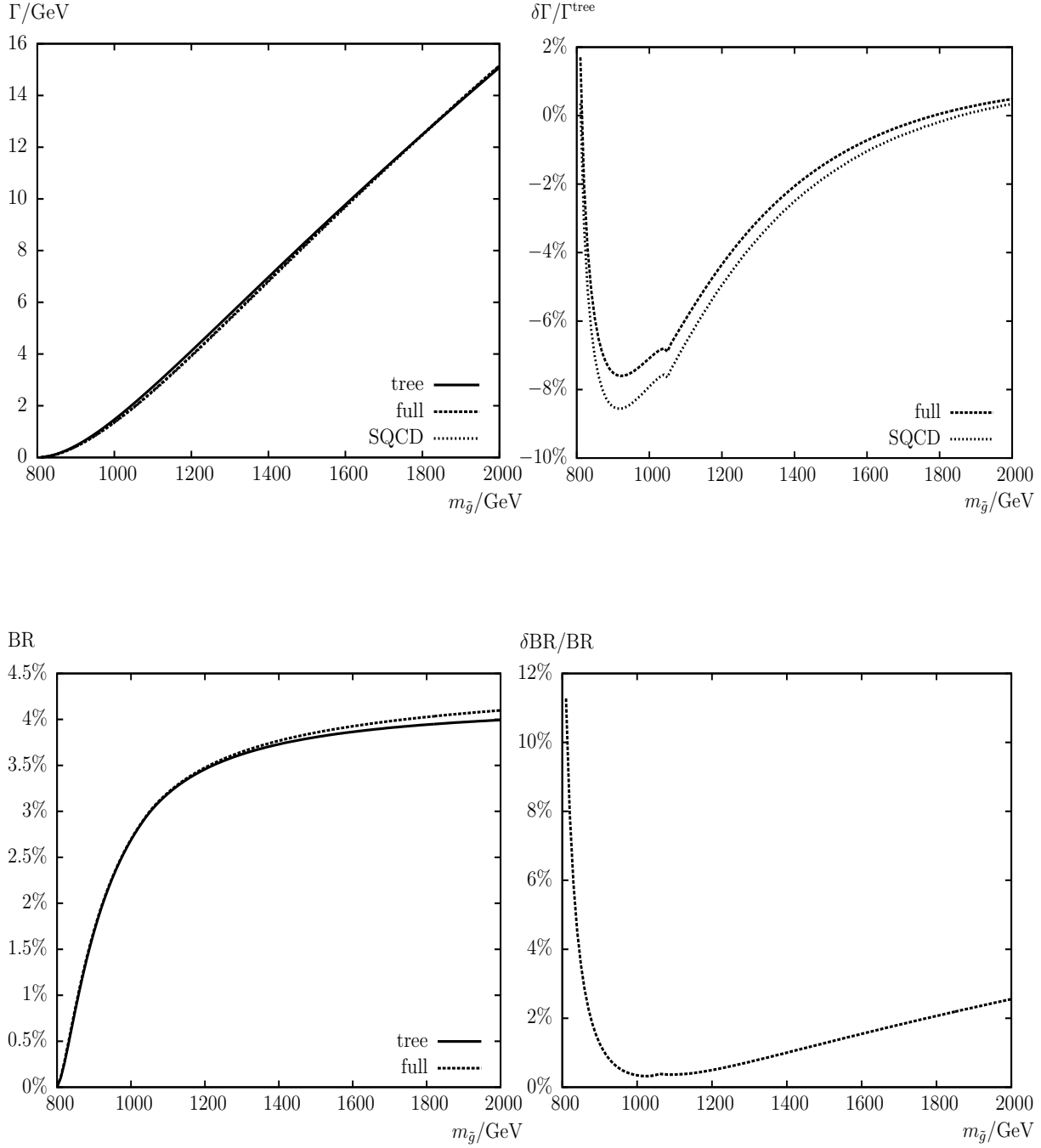


Figure 8: $\Gamma(\tilde{g} \rightarrow \tilde{c}_2 c)$. Tree-level (“tree”) and full one-loop (“full”) corrected decay widths are shown with the parameters chosen according to \mathcal{S} (see Tab. 1), with $m_{\tilde{g}}$ varied. The upper left plot shows the decay width, the upper right plot shows the relative size of the corrections. Also shown are the pure SQCD corrections (“SQCD”). The lower left plot shows the BR, the lower right plot shows the relative size of the BR.

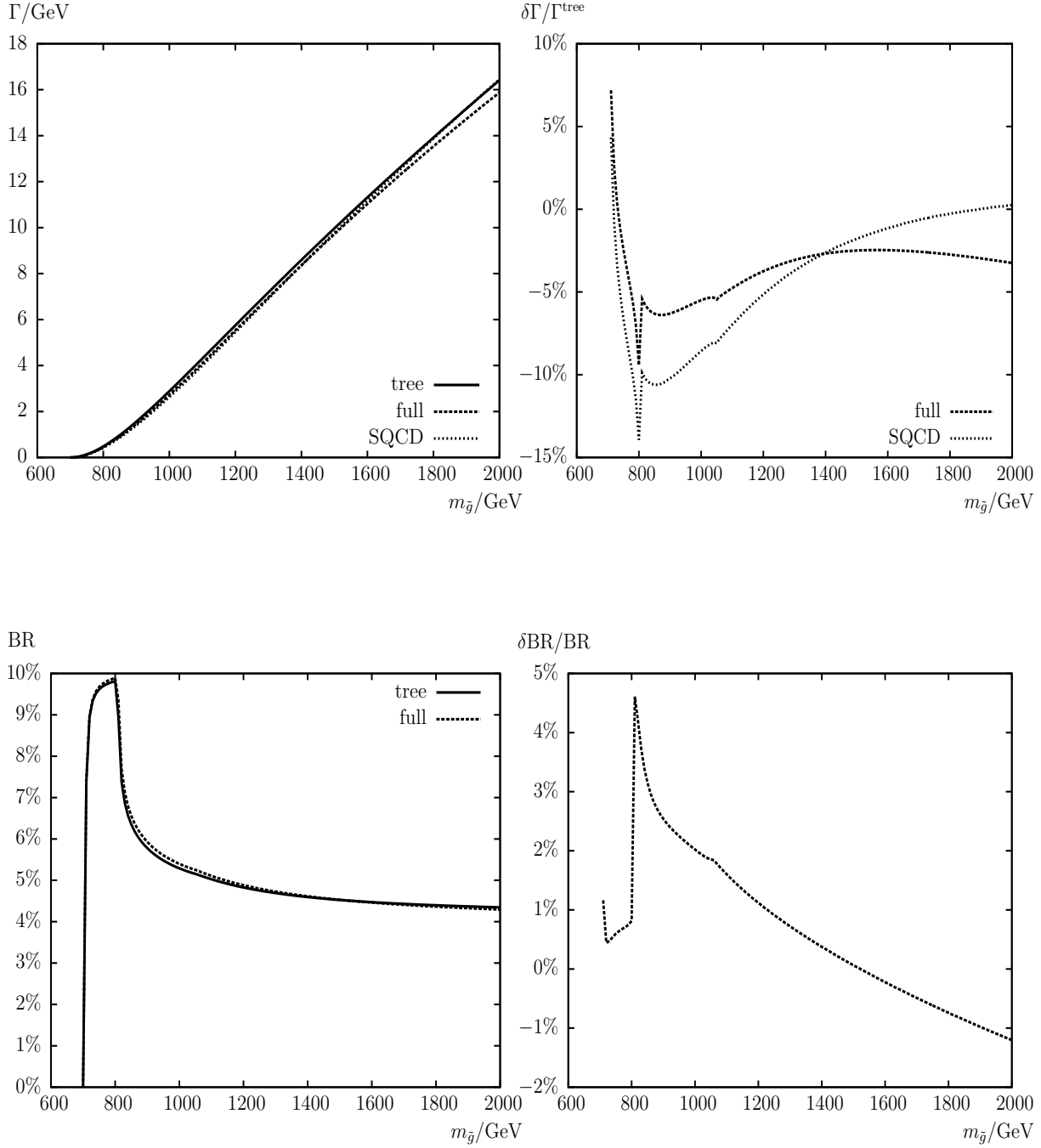


Figure 9: $\Gamma(\tilde{g} \rightarrow \tilde{s}_1 s)$. Tree-level (“tree”) and full one-loop (“full”) corrected decay widths are shown with the parameters chosen according to \mathcal{S} (see Tab. 1), with $m_{\tilde{g}}$ varied. The upper left plot shows the decay width, the upper right plot shows the relative size of the corrections. Also shown are the pure SQCD corrections (“SQCD”). The lower left plot shows the BR, the lower right plot shows the relative size of the BR.

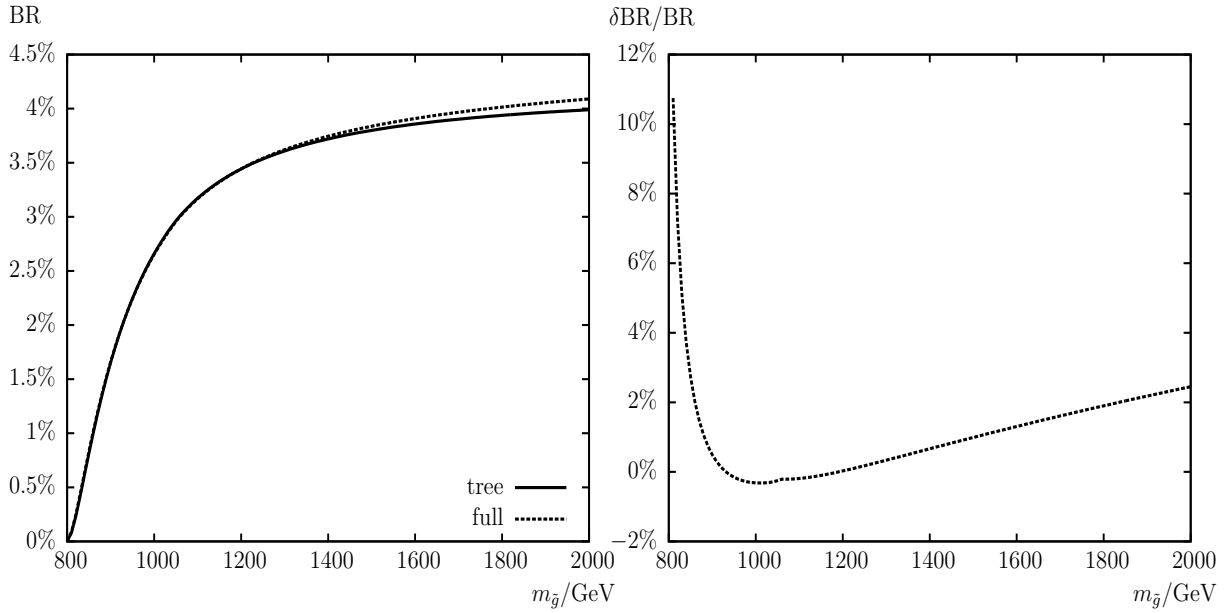
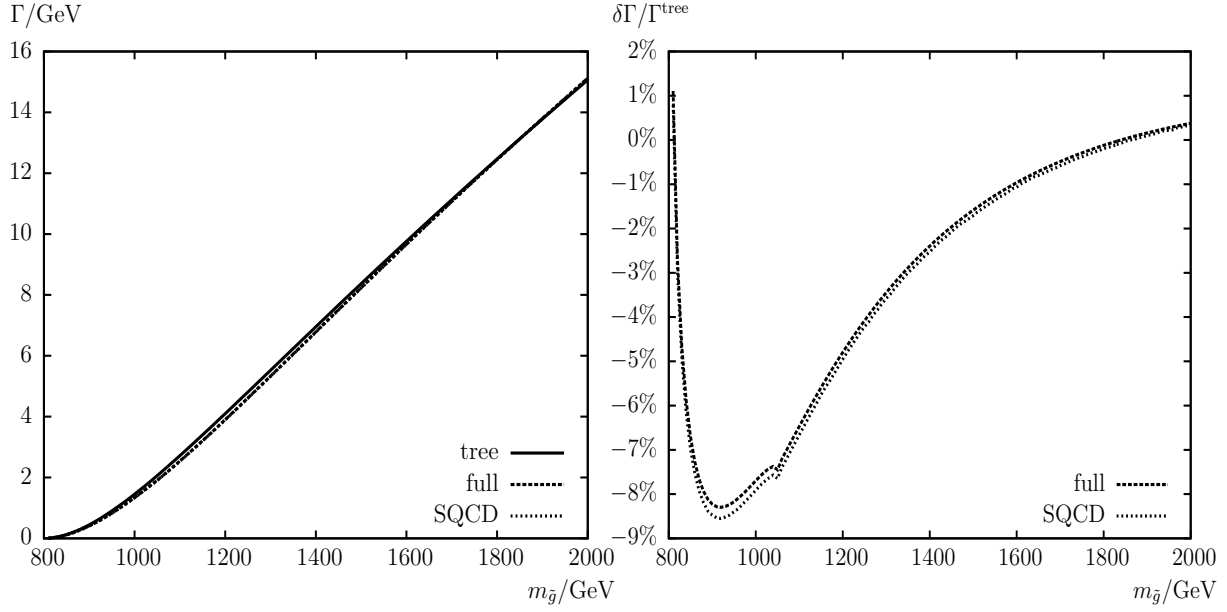


Figure 10: $\Gamma(\tilde{g} \rightarrow \tilde{s}_2 s)$. Tree-level (“tree”) and full one-loop (“full”) corrected decay widths are shown with the parameters chosen according to \mathcal{S} (see Tab. 1), with $m_{\tilde{g}}$ varied. The upper left plot shows the decay width, the upper right plot shows the relative size of the corrections. Also shown are the pure SQCD corrections (“SQCD”). The lower left plot shows the BR, the lower right plot shows the relative size of the BR.

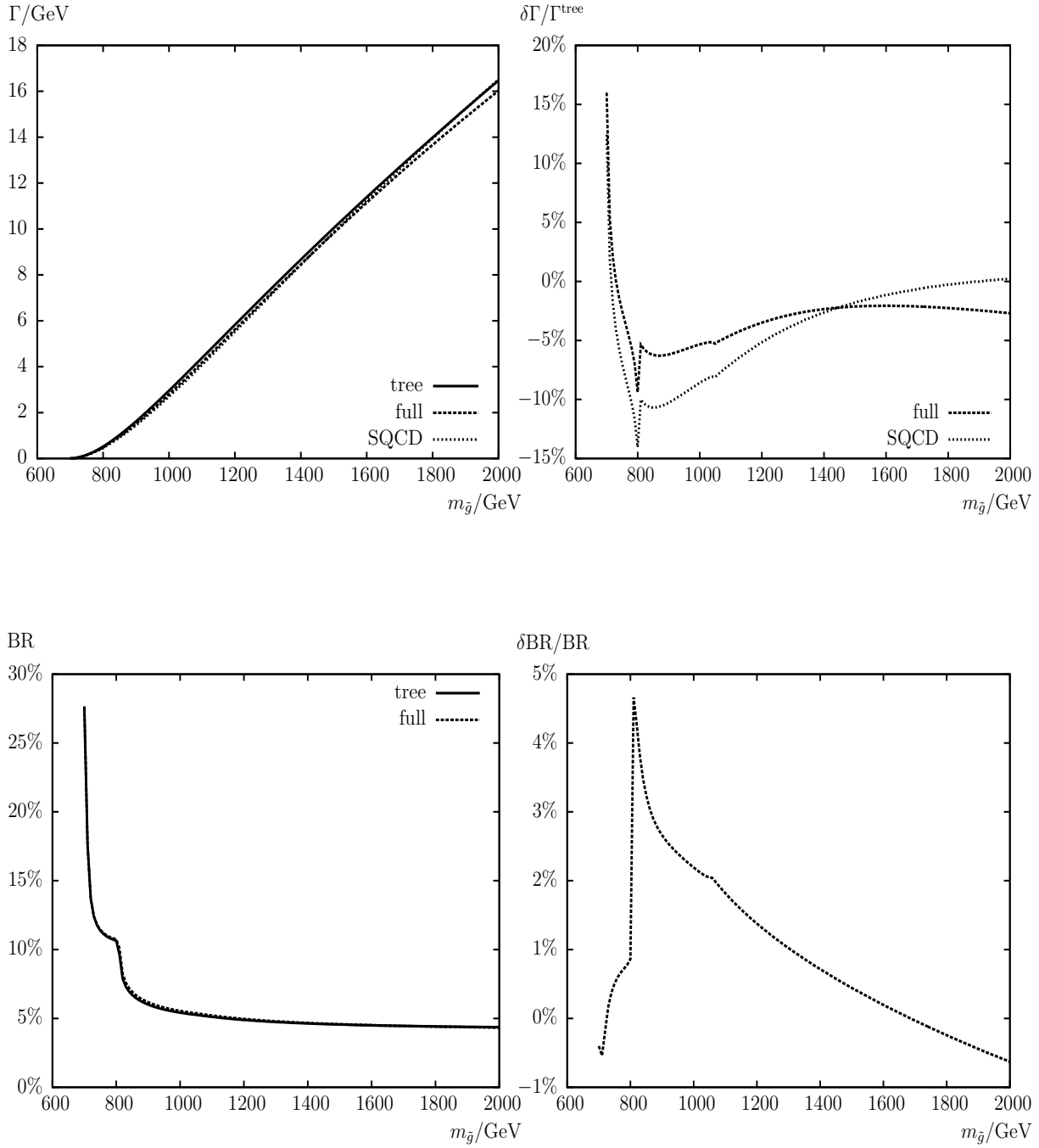


Figure 11: $\Gamma(\tilde{g} \rightarrow \tilde{u}_1 u)$. Tree-level (“tree”) and full one-loop (“full”) corrected decay widths are shown with the parameters chosen according to \mathcal{S} (see Tab. 1), with $m_{\tilde{g}}$ varied. The upper left plot shows the decay width, the upper right plot shows the relative size of the corrections. Also shown are the pure SQCD corrections (“SQCD”). The lower left plot shows the BR, the lower right plot shows the relative size of the BR.

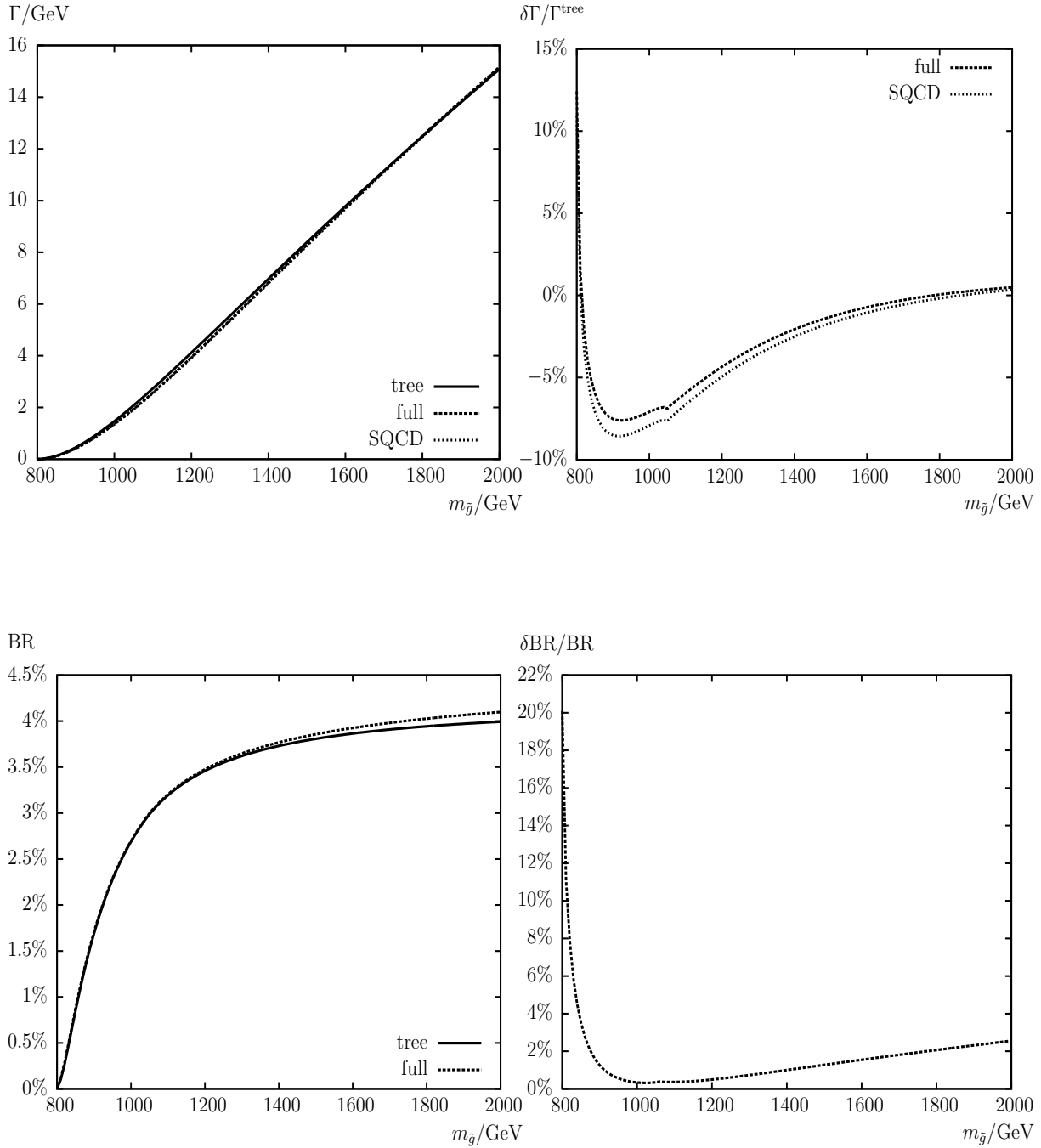


Figure 12: $\Gamma(\tilde{g} \rightarrow \tilde{u}_2 u)$. Tree-level (“tree”) and full one-loop (“full”) corrected decay widths are shown with the parameters chosen according to \mathcal{S} (see Tab. 1), with $m_{\tilde{g}}$ varied. The upper left plot shows the decay width, the upper right plot shows the relative size of the corrections. Also shown are the pure SQCD corrections (“SQCD”). The lower left plot shows the BR, the lower right plot shows the relative size of the BR.

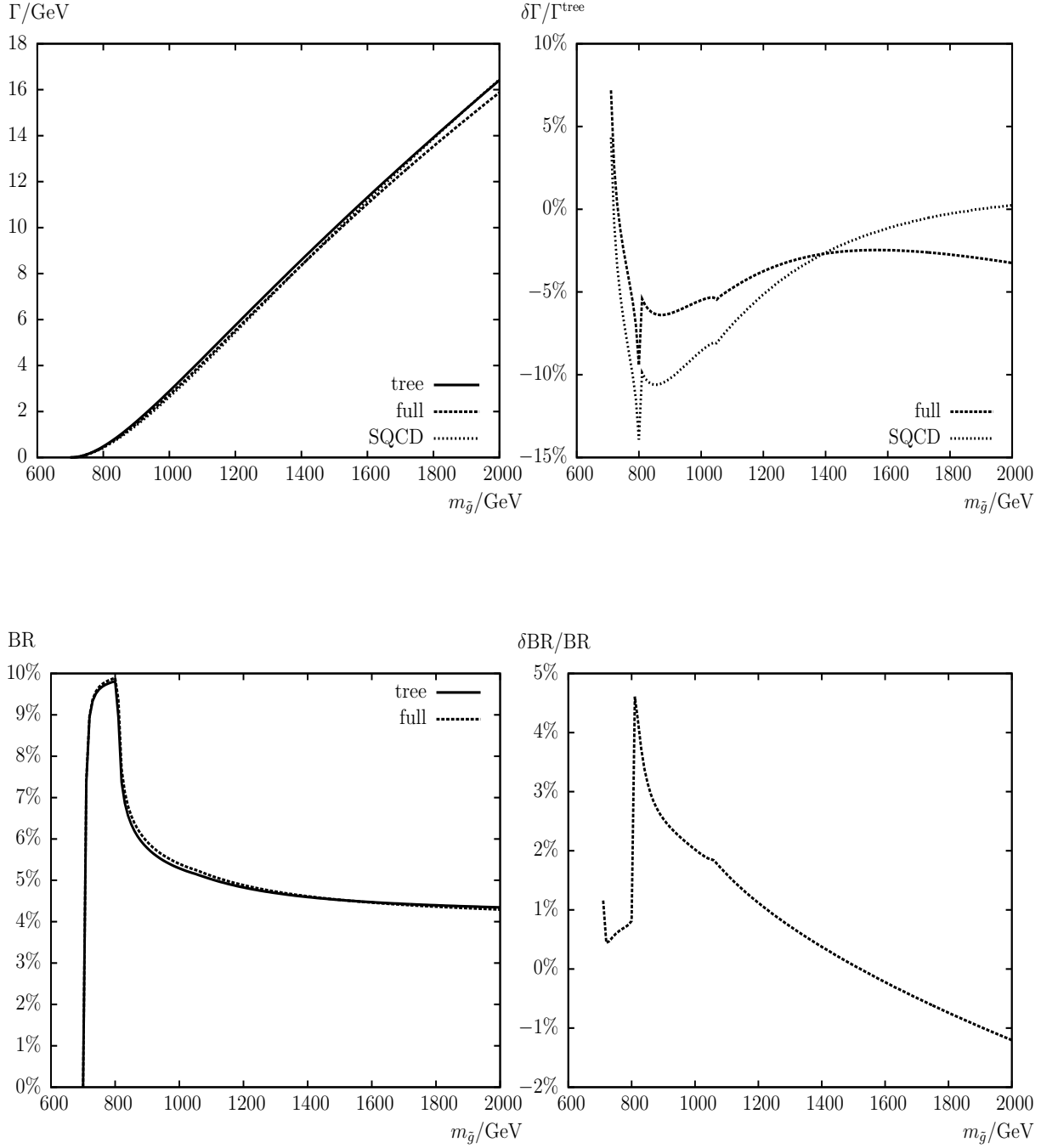


Figure 13: $\Gamma(\tilde{g} \rightarrow \tilde{d}_1 d)$. Tree-level (“tree”) and full one-loop (“full”) corrected decay widths are shown with the parameters chosen according to \mathcal{S} (see Tab. 1), with $m_{\tilde{g}}$ varied. The upper left plot shows the decay width, the upper right plot shows the relative size of the corrections. Also shown are the pure SQCD corrections (“SQCD”). The lower left plot shows the BR, the lower right plot shows the relative size of the BR.

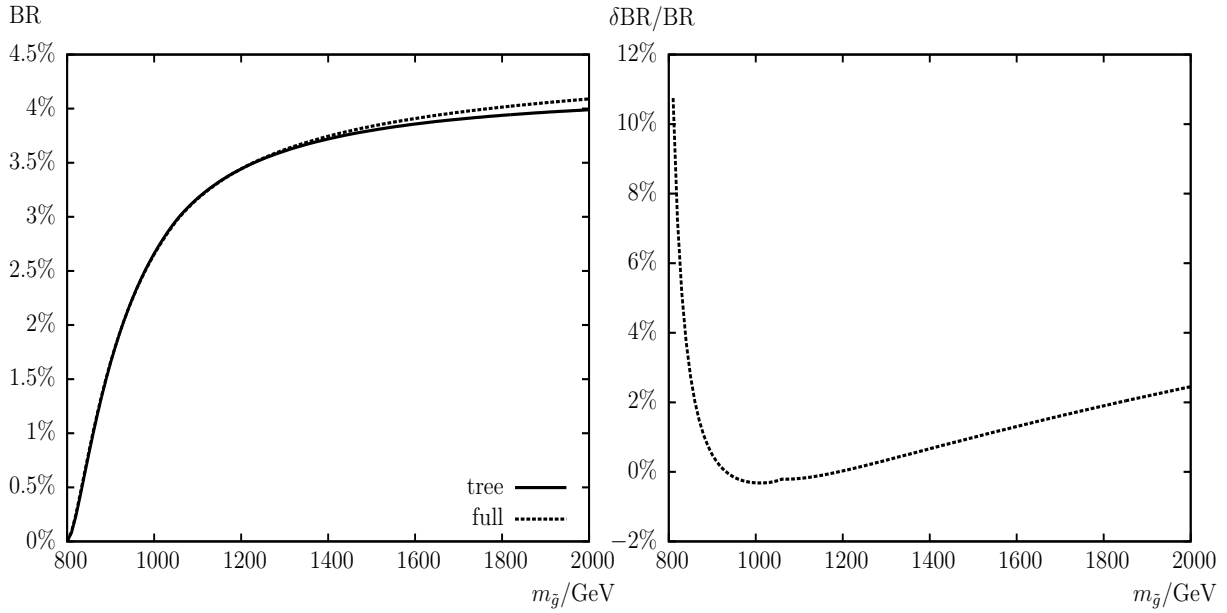
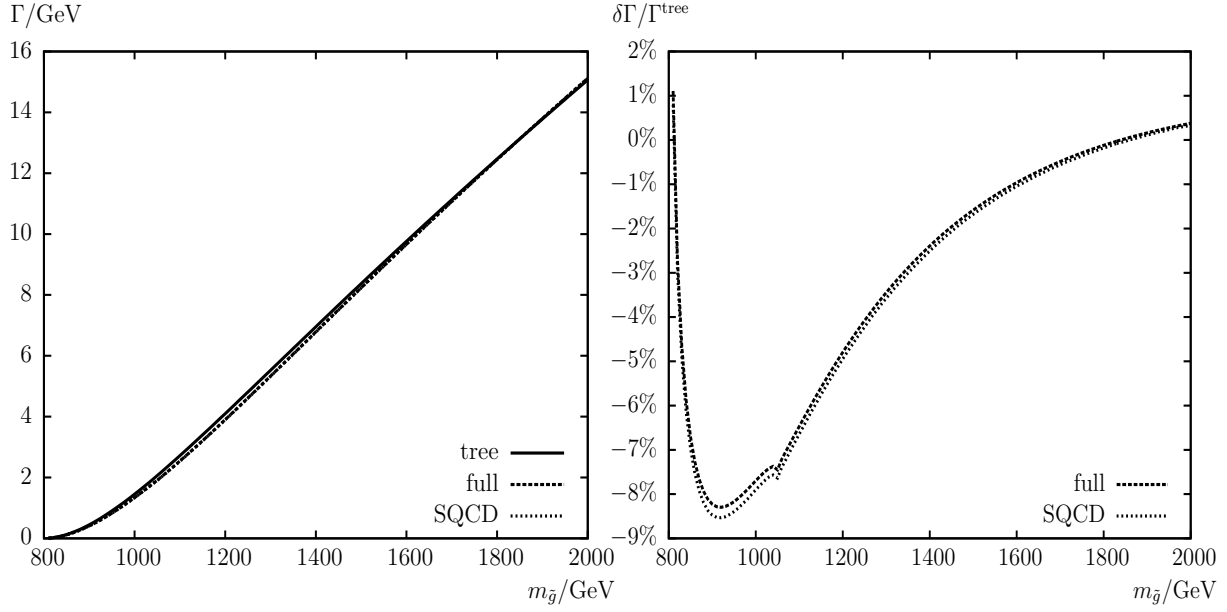


Figure 14: $\Gamma(\tilde{g} \rightarrow \tilde{d}_2 d)$. Tree-level (“tree”) and full one-loop (“full”) corrected decay widths are shown with the parameters chosen according to \mathcal{S} (see Tab. 1), with $m_{\tilde{g}}$ varied. The upper left plot shows the decay width, the upper right plot shows the relative size of the corrections. Also shown are the pure SQCD corrections (“SQCD”). The lower left plot shows the BR, the lower right plot shows the relative size of the BR.

4.3 Full one-loop results for varying $\varphi_{\tilde{g}}$

In this subsection we analyze the various decay widths and branching ratios as a function of $\varphi_{\tilde{g}}$. The other parameters are chosen according to Tab. 1.

When performing an analysis involving complex parameters it should be noted that the results for physical observables are affected only by certain combinations of the complex phases of the parameters μ , the trilinear couplings A_t, A_b, \dots , and the gaugino mass parameters M_1, M_2, M_3 [25, 38]. It is possible, for instance, to rotate the phase φ_{M_2} away, and we remain with φ_{M_1} and $\varphi_{M_3} \equiv \varphi_{\tilde{g}}$ as independent physical phases. Experimental constraints on the (combinations of) complex phases arise in particular from their contributions to electric dipole moments of heavy quarks [39], of the electron and the neutron (see Refs. [40, 41] and references therein), and of deuteron [42], Refs. [40, 43, 44] for reviews. The phase of the gluino mass parameter remains relatively weakly constrained. Since our decaying particle is the gluino we focus here on the dependence on $\varphi_{\tilde{g}}$ and set all other phases to zero. Analyses of the full one-loop effects of SUSY decays on $\varphi_{A_b}, \varphi_{A_t}$ and φ_{M_1} can be found in Refs. [15, 16, 27], respectively.

Since now the complex phase of M_3 can appear in the couplings, two effects arise: first a difference between $\Gamma(\tilde{g} \rightarrow \tilde{q}_i^\dagger q)$ and $\Gamma(\tilde{g} \rightarrow \tilde{q}_i \bar{q})$ is observed, and consequently we now show the results separately for these two decay channels (but stick to the notation “ $\tilde{g} \rightarrow \tilde{q}_i q$ ” when referring in general to a plot). These differences arise naturally from the combination of an imaginary (absorptive) part of a decay diagram and a complex coupling. As required, we always find $\Gamma(\tilde{g} \rightarrow \tilde{q}_i^\dagger q)|_{\varphi_{\tilde{g}}} = \Gamma(\tilde{g} \rightarrow \tilde{q}_i \bar{q})|_{-\varphi_{\tilde{g}}}$. A second source of this type of contributions comes from absorptive parts of self-energy type corrections on external legs (called “absorptive self-energy contributions” from now on), and they also have been included according to the formulas given in Sect. 2.3. For $\varphi_{\tilde{g}} = 0, \pi, 2\pi$ these “absorptive effects” vanish (by construction).

As before we show the decays in Fig. 15 – 26. The arrangement of the panels is the same as in the previous subsection (but leaving out the pure SQCD corrections). According to Tab. 1 we choose $m_{\tilde{g}} = 1200$ GeV, which is substantially larger than the squark masses. Accordingly we expect again that $\text{BR}(\tilde{g} \rightarrow \tilde{q}_1 q) + \text{BR}(\tilde{g} \rightarrow \tilde{q}_2 q) \sim 1/6$, with possible deviations in the decays involving scalar tops, where the mass variation is maximal.

The results for $\tilde{g} \rightarrow \tilde{t}_1 t$ are shown in Fig. 15, where the results are given as a function of $\varphi_{\tilde{g}}$. One can see that both the decay widths as well as the size of the corrections to it vary substantially with $\varphi_{\tilde{g}}$. While the widths ranges between ~ 8 GeV and ~ 4 GeV, the corrections vary between -8.5% and -2.5% in our numerical scenario \mathcal{S} , where also a small difference between $\tilde{g} \rightarrow \tilde{t}_1^\dagger t$ and $\tilde{g} \rightarrow \tilde{t}_1 \bar{t}$ can be observed. The BR’s vary correspondingly from $\sim 8.0\%$ to $\sim 4\%$, where the size of the loop effects in \mathcal{S} goes from -4% to $\sim +2\%$, again with a small visible difference between $\tilde{g} \rightarrow \tilde{t}_1^\dagger t$ and $\tilde{g} \rightarrow \tilde{t}_1 \bar{t}$. The second channel involving scalar tops, $\tilde{g} \rightarrow \tilde{t}_2 t$, is shown in Fig. 16. In agreement with Fig. 4 the decay width is substantially smaller than for $\tilde{g} \rightarrow \tilde{t}_1 t$, largely due to the reduced phase space, varying between ~ 1 GeV and ~ 3.5 GeV. The difference between $\Gamma(\tilde{g} \rightarrow \tilde{t}_2^\dagger t)$ and $\Gamma(\tilde{g} \rightarrow \tilde{t}_2 \bar{t})$ is clearly visible. The loop corrections range from $+4\%$ to -10% , with a clear symmetry between $\tilde{g} \rightarrow \tilde{t}_2^\dagger t$ and $\tilde{g} \rightarrow \tilde{t}_2 \bar{t}$. Correspondingly, the $\text{BR}(\tilde{g} \rightarrow \tilde{t}_2 t)$ reach values between $\sim 1\%$ and $\sim 3.5\%$ with a variation of $+8\%$ to -6% . The sum of the four BR’s is close to but always a bit smaller than $\sim 1/6$ due to the non-negligible effects of the scalar top masses

and mixings.

For all other decay modes, i.e. $\tilde{g} \rightarrow \tilde{q}_i q$ with $q \neq t$, the mass and mixing effects are substantially smaller.⁹ Within \mathcal{S} we find $\Gamma(\tilde{g} \rightarrow \tilde{q}_1 q, q \neq t)$ (shown in Figs. 17, 19, 21, 23, 25) at the level of ~ 5.5 GeV, where small variations depend on the squark flavor. Also the required symmetry of $\Gamma(\tilde{g} \rightarrow \tilde{q}_1^\dagger q, q \neq t)|_{\varphi_{\tilde{g}}} = \Gamma(\tilde{g} \rightarrow \tilde{q}_1 \bar{q}, q \neq t)|_{-\varphi_{\tilde{g}}}$ is clearly visible, and similarly for the BR's and the size of the loop corrections. While the size of the one-loop corrections vary between -1% and -6% in the case of $\tilde{g} \rightarrow \tilde{b}_1 b$, they are found to be within $\sim -3\%$ and $\sim -4.5\%$ for the other flavors. The corresponding BR's are found at the level of $\sim 5\%$ with less than $\pm 0.25\%$ of variation. The relative corrections in \mathcal{S} are at the few per-cent level at most.

The results for the decay modes to the heavier scalar quarks, $\tilde{g} \rightarrow \tilde{q}_2 q, q \neq t$, shown in Figs. 18, 20, 22, 24, 26, are also very similar, again with a visible difference between $\tilde{g} \rightarrow \tilde{q}_2^\dagger q$ and $\tilde{g} \rightarrow \tilde{q}_2 \bar{q}, q \neq t$. The widths are ~ 4 GeV with a small phase dependence. The size of the one-loop corrections vary around -5% for $\tilde{g} \rightarrow \tilde{b}_2 b$, $\sim -4.35\%$ for $\tilde{g} \rightarrow \tilde{q}_2 q, q = c, u$, and $\sim -4.85\%$ for $\tilde{g} \rightarrow \tilde{q}_2 q, q = s, d$. The BR's for all flavors are found at $\sim 3.5\%$ with loop corrections at the per-cent level. As “expected”, for all flavors we find $\text{BR}(\tilde{g} \rightarrow \tilde{q}_1 q) + \text{BR}(\tilde{g} \rightarrow \tilde{q}_2 q) \sim 1/6$.

4.4 The one-loop decays $\tilde{g} \rightarrow \tilde{\chi}_k^0 g$

In Figs. 27 – 30 we present the variation of $\Gamma(\tilde{g} \rightarrow \tilde{\chi}_k^0 g), (k = 1, 2, 3, 4)$ as a function of $m_{\tilde{g}}$ and $\varphi_{\tilde{g}}$ in \mathcal{S} , see Tab. 1. The structure at $m_{\tilde{g}} \approx 1054.6$ in Fig. 27 and Fig. 28 is the vertex production threshold $m_{\tilde{g}} = m_{\tilde{t}_2} + m_t$. In Fig. 29 and Fig. 30 the dip at $m_{\tilde{g}} \approx 699.2$ GeV stems from the vertex production threshold $m_{\tilde{g}} = m_{\tilde{c}_1} + m_c$, the peak at $m_{\tilde{g}} \approx 809.3$ GeV is the vertex production threshold $m_{\tilde{g}} = m_{\tilde{t}_1} + m_t$.

With our choice of parameters, see Tab. 1, we find the neutralino masses at $\sim 151, 206, 218, 338$ GeV, i.e. relatively similar with respect to the larger gluino mass. The size of the decay widths is very small for all four neutralinos with respect to the hadronic final states discussed in the previous subsection. The largest values are reached for $\tilde{g} \rightarrow \tilde{\chi}_2^0 g$, going up to ~ 0.007 GeV. The dependence on $m_{\tilde{g}}$ is very similar, as expected from the large gap between neutralino and gluino mass. We see a threshold on-set, going up to the maximum values around 800 GeV. Due to the smallness of the decay widths the corresponding branching ratios are negligible in \mathcal{S} .¹⁰ However, in a situation where the gluino is lighter than all scalar quarks these loop-induced two-body decay modes can become relevant and may constitute a significant source for $\tilde{\chi}_1^0$ production at the LHC (which could be used to measure the properties of the SUSY CDM candidate). In such a situation, of course, also three particle final states will be relevant, which are, however, beyond the scope of this paper.

⁹ Especially the tree-level results depends strongly on the scalar quark mass splitting $m_q X_q$ (see Eqs. (4), (5)) via $U_{\tilde{q}_{ij}} e^{i\varphi_{\tilde{g}}/2}$ and is therefore nearly constant with respect to $\varphi_{\tilde{g}}$ for $q \neq t$.

¹⁰ They are not included in the calculation of the total decay widths shown in Sect. 4.5.

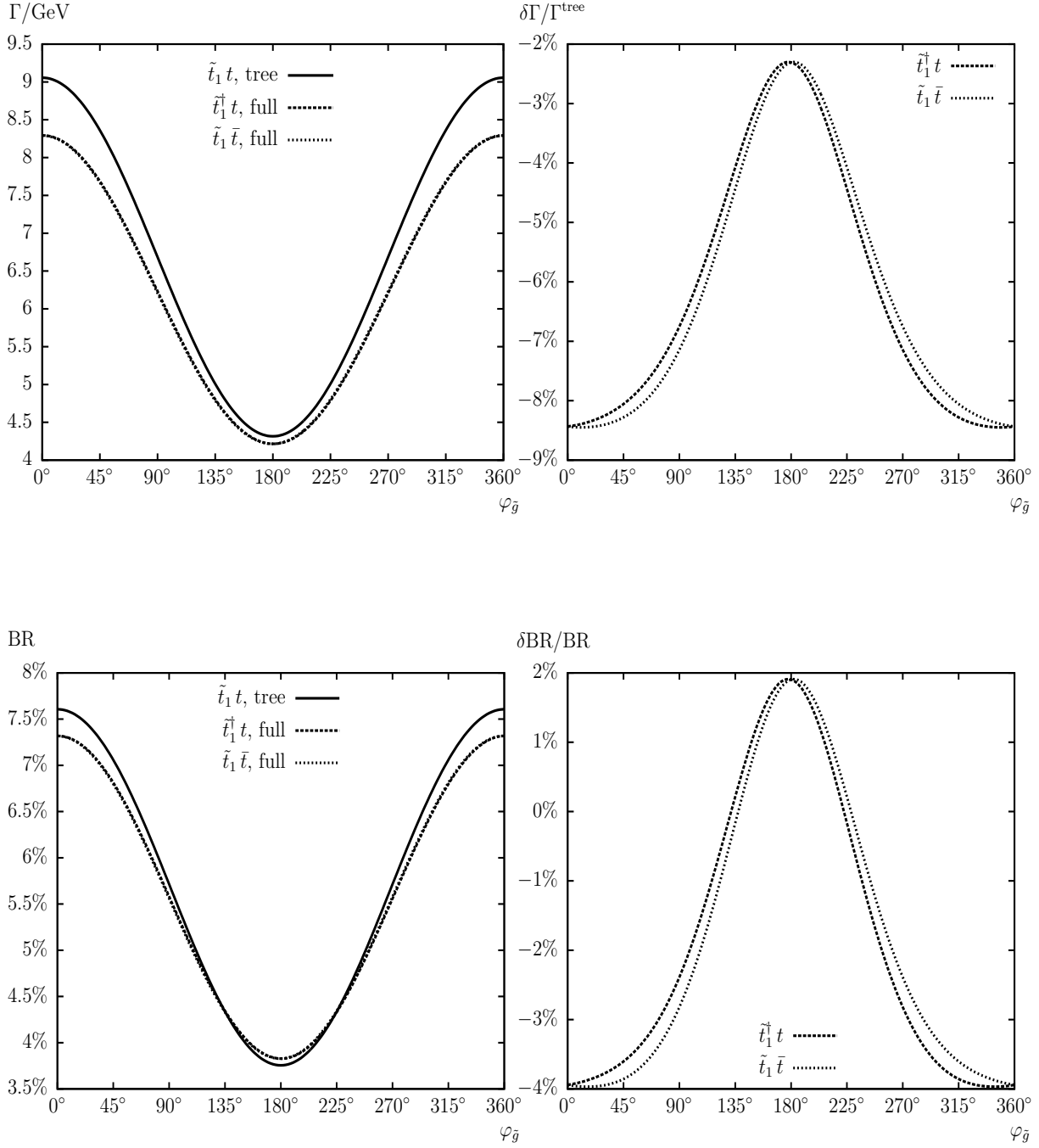


Figure 15: $\Gamma(\tilde{g} \rightarrow \tilde{t}_1 t)$. Tree-level (“tree”) and full one-loop (“full”) corrected decay widths (including absorptive self-energy contributions) are shown. The parameters are chosen according to \mathcal{S} (see Tab. 1), with $\varphi_{\tilde{g}}$ varied. The upper left plot shows the decay width, the upper right plot shows the relative size of the corrections. The lower left plot shows the BR, the lower right plot shows the relative size of the BR.

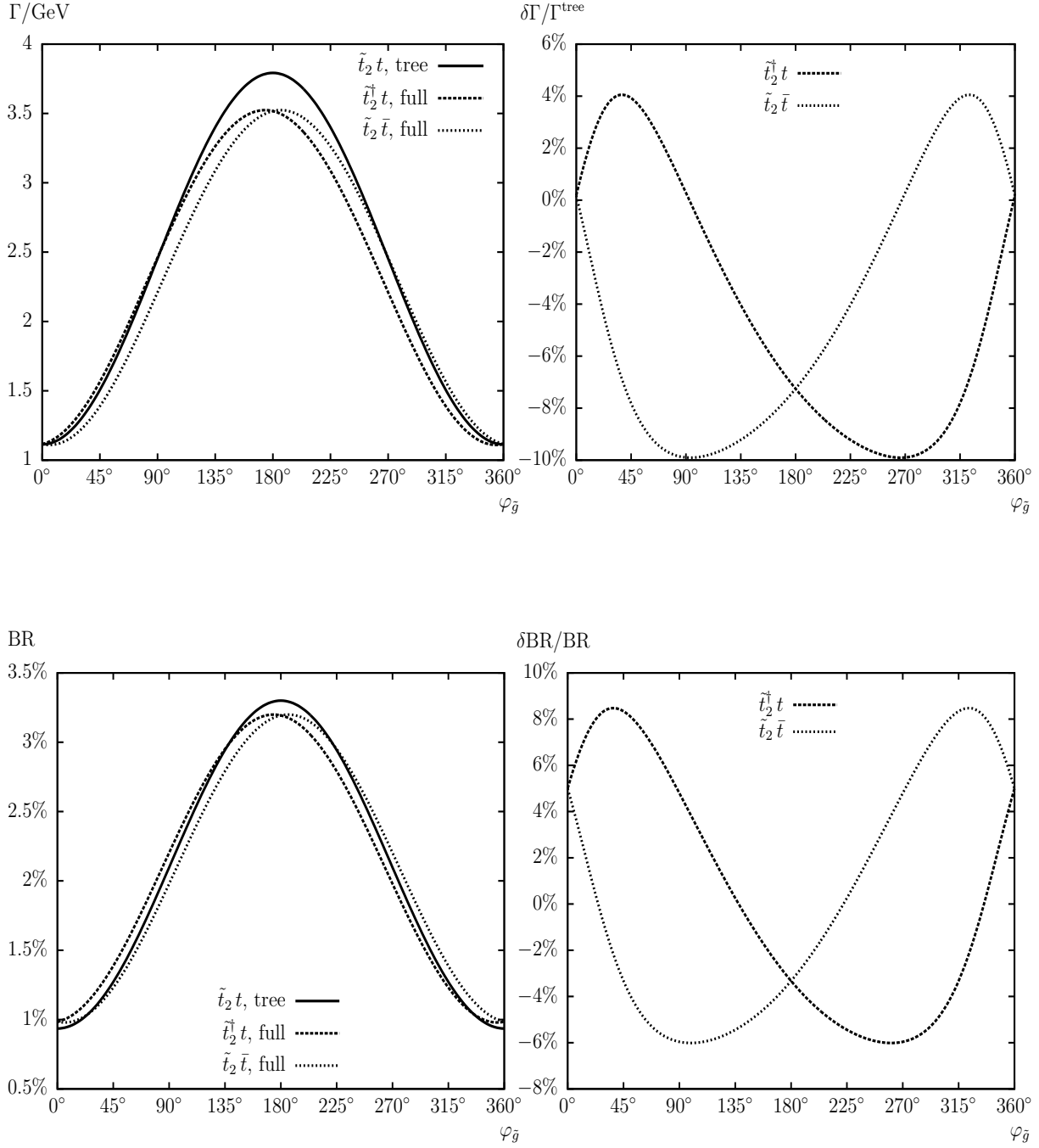


Figure 16: $\Gamma(\tilde{g} \rightarrow \tilde{t}_2 t)$. Tree-level (“tree”) and full one-loop (“full”) corrected decay widths (including absorptive self-energy contributions) are shown. The parameters are chosen according to \mathcal{S} (see Tab. 1), with $\varphi_{\tilde{g}}$ varied. The upper left plot shows the decay width, the upper right plot shows the relative size of the corrections. The lower left plot shows the BR, the lower right plot shows the relative size of the BR.

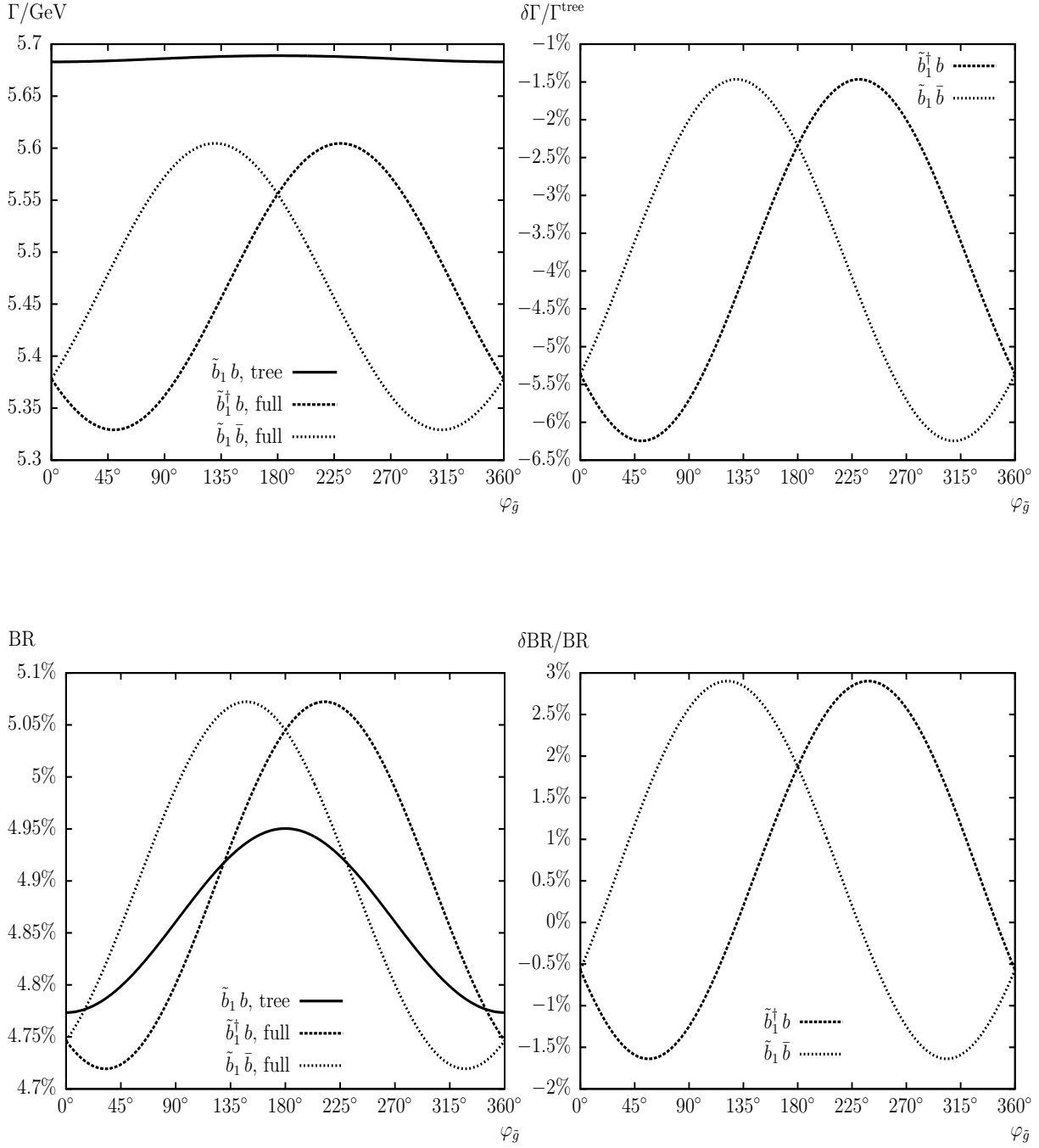


Figure 17: $\Gamma(\tilde{g} \rightarrow \tilde{b}_1 b)$. Tree-level (“tree”) and full one-loop (“full”) corrected decay widths (including absorptive self-energy contributions) are shown. The parameters are chosen according to \mathcal{S} (see Tab. 1), with $\varphi_{\tilde{g}}$ varied. The upper left plot shows the decay width, the upper right plot shows the relative size of the corrections. The lower left plot shows the BR, the lower right plot shows the relative size of the BR.

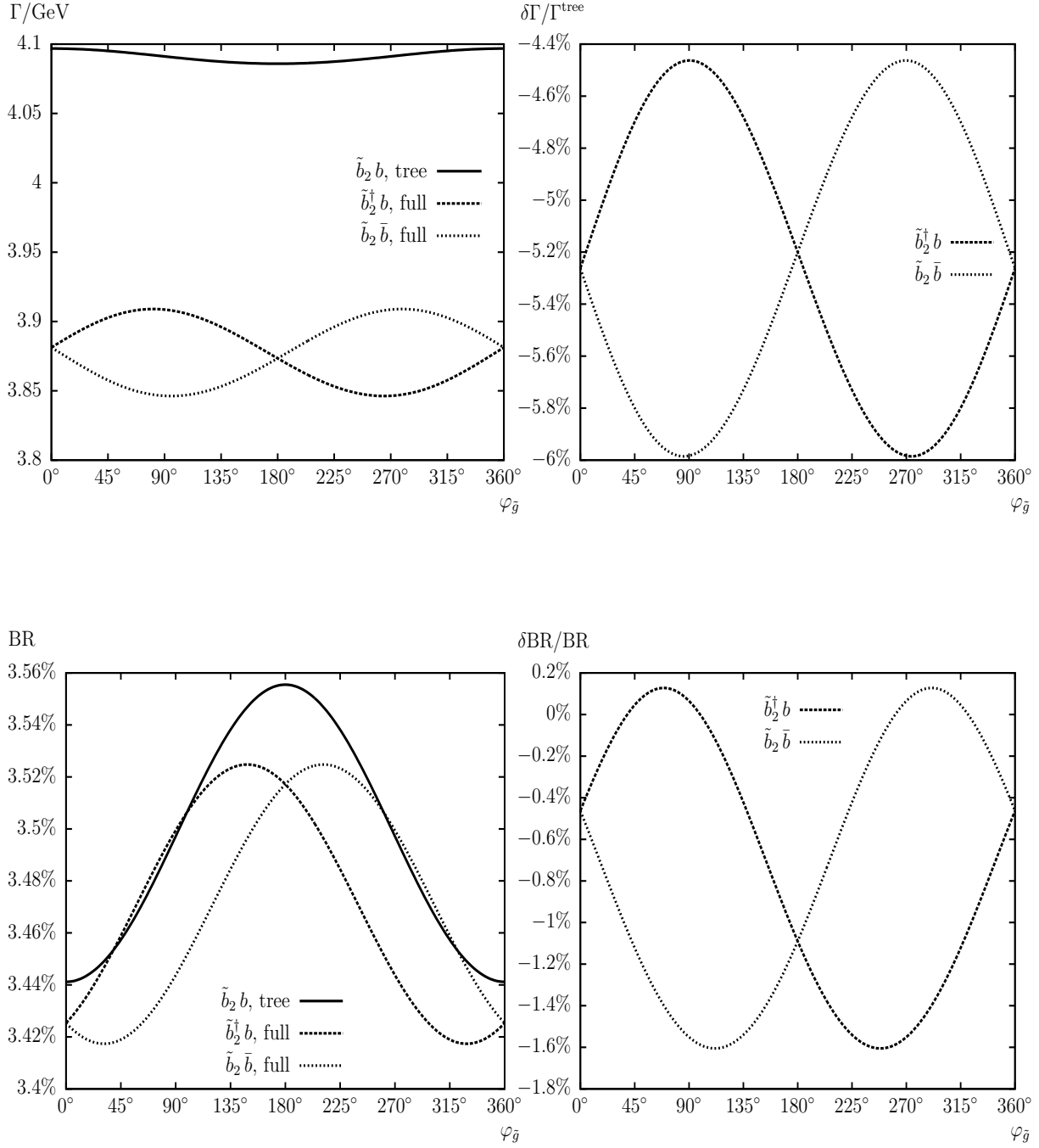


Figure 18: $\Gamma(\tilde{g} \rightarrow \tilde{b}_2 b)$. Tree-level (“tree”) and full one-loop (“full”) corrected decay widths (including absorptive self-energy contributions) are shown. The parameters are chosen according to \mathcal{S} (see Tab. 1), with $\varphi_{\tilde{g}}$ varied. The upper left plot shows the decay width, the upper right plot shows the relative size of the corrections. The lower left plot shows the BR, the lower right plot shows the relative size of the BR.

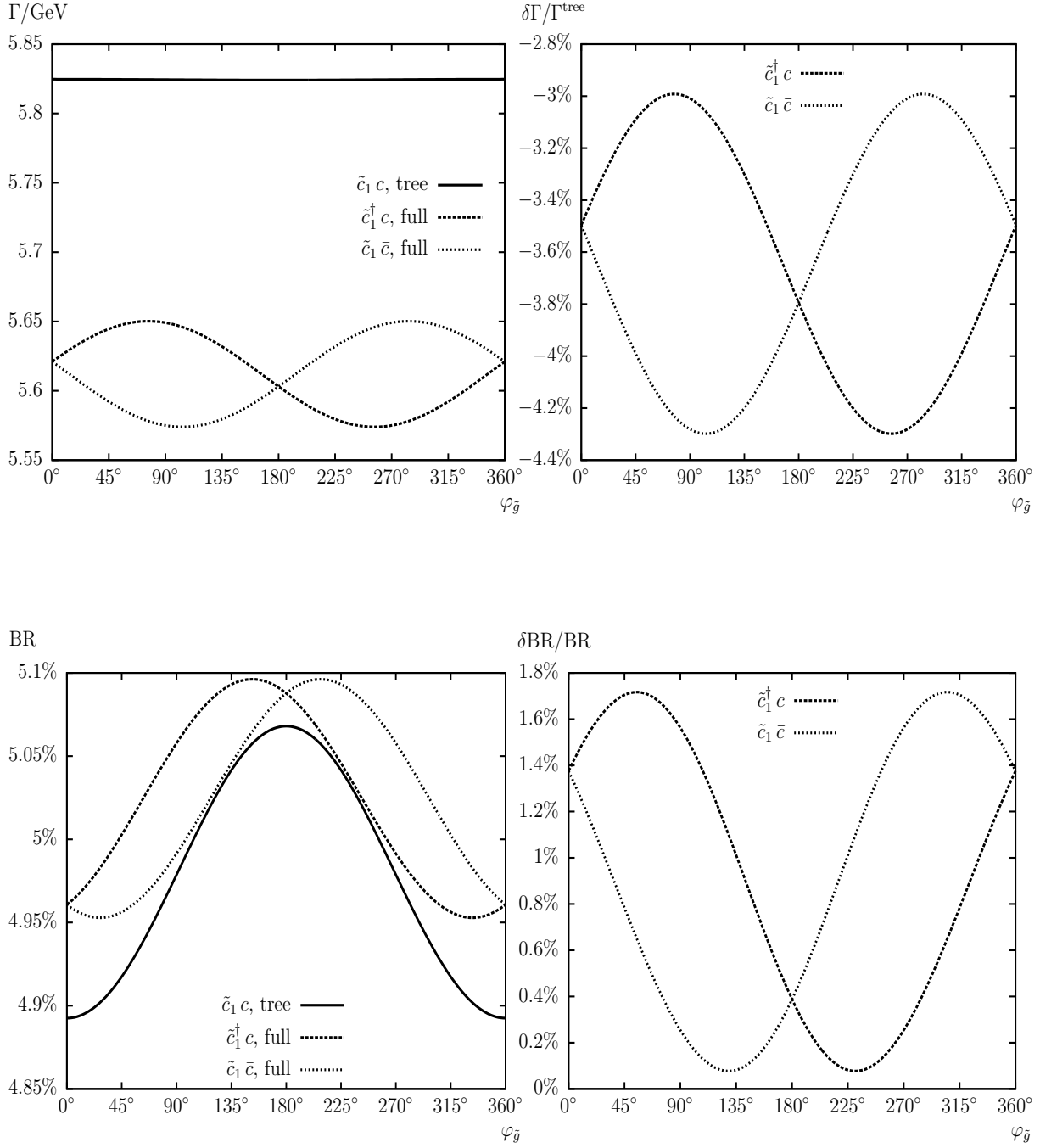


Figure 19: $\Gamma(\tilde{g} \rightarrow \tilde{c}_1 c)$. Tree-level (“tree”) and full one-loop (“full”) corrected decay widths (including absorptive self-energy contributions) are shown. The parameters are chosen according to \mathcal{S} (see Tab. 1), with $\varphi_{\tilde{g}}$ varied. The upper left plot shows the decay width, the upper right plot shows the relative size of the corrections. The lower left plot shows the BR, the lower right plot shows the relative size of the BR.

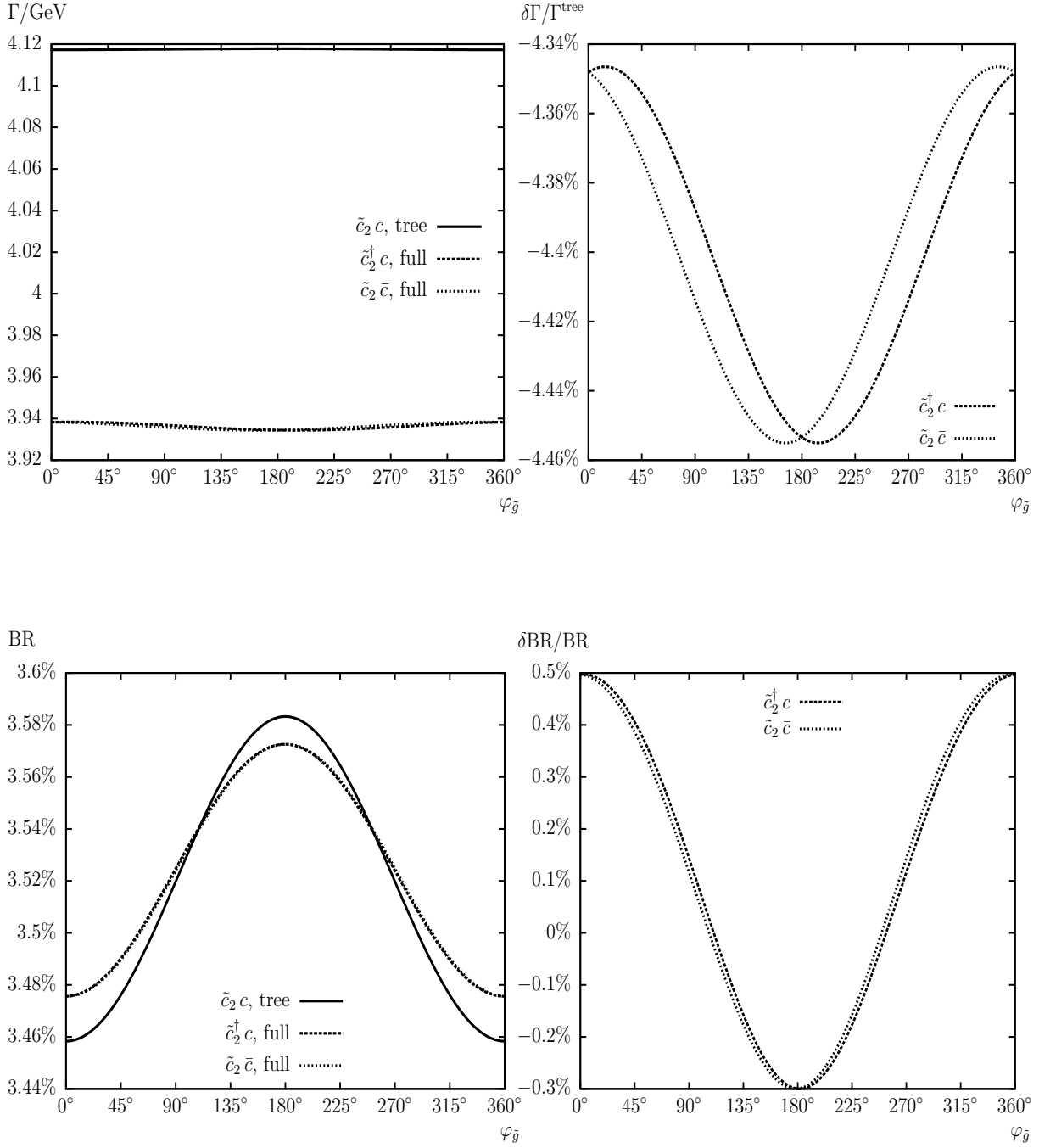


Figure 20: $\Gamma(\tilde{g} \rightarrow \tilde{c}_2 c)$. Tree-level (“tree”) and full one-loop (“full”) corrected decay widths (including absorptive self-energy contributions) are shown. The parameters are chosen according to \mathcal{S} (see Tab. 1), with $\varphi_{\tilde{g}}$ varied. The upper left plot shows the decay width, the upper right plot shows the relative size of the corrections. The lower left plot shows the BR, the lower right plot shows the relative size of the BR.

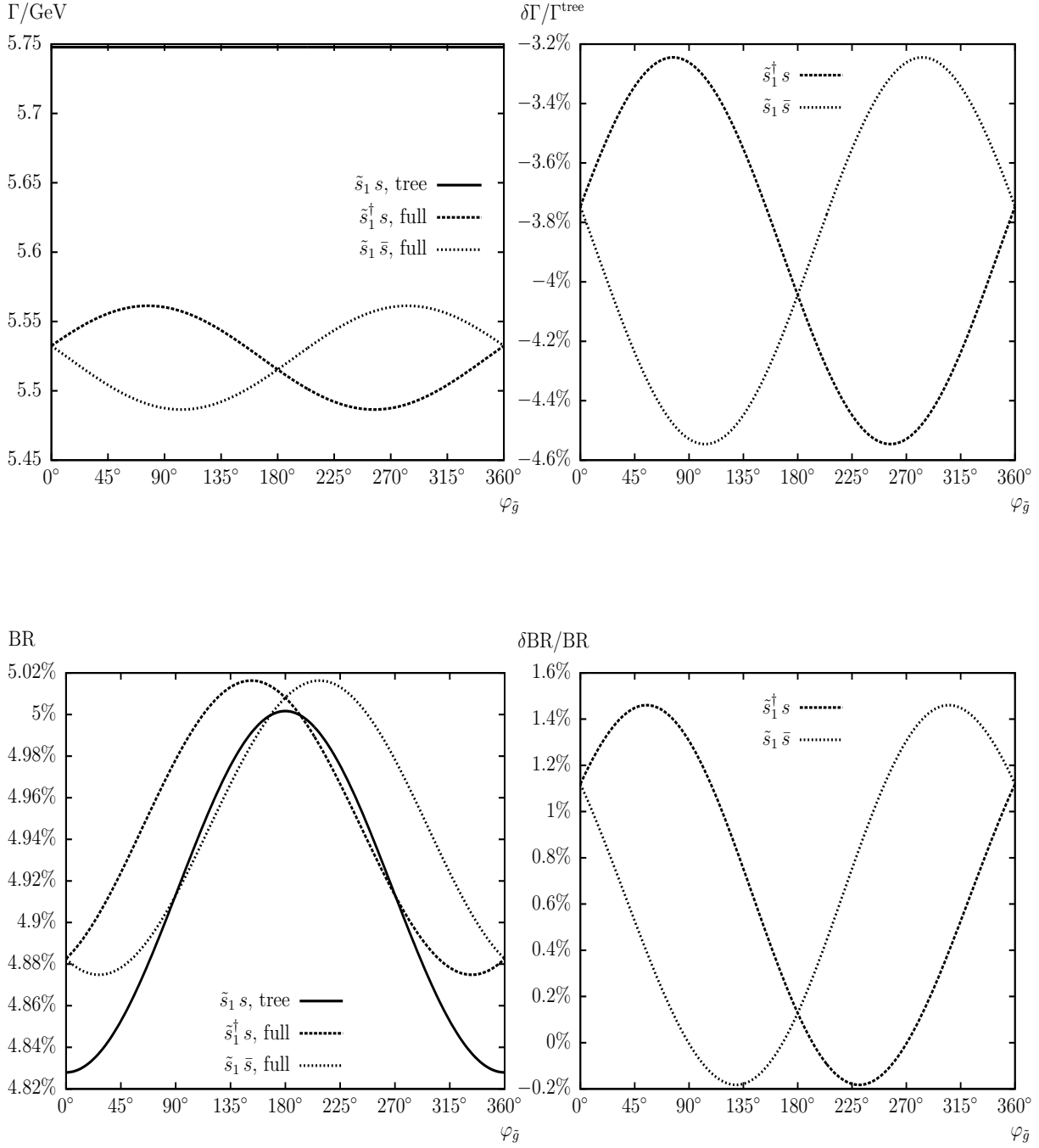


Figure 21: $\Gamma(\tilde{g} \rightarrow \tilde{s}_1 s)$. Tree-level (“tree”) and full one-loop (“full”) corrected decay widths (including absorptive self-energy contributions) are shown. The parameters are chosen according to \mathcal{S} (see Tab. 1), with $\varphi_{\tilde{g}}$ varied. The upper left plot shows the decay width, the upper right plot shows the relative size of the corrections. The lower left plot shows the BR, the lower right plot shows the relative size of the BR.

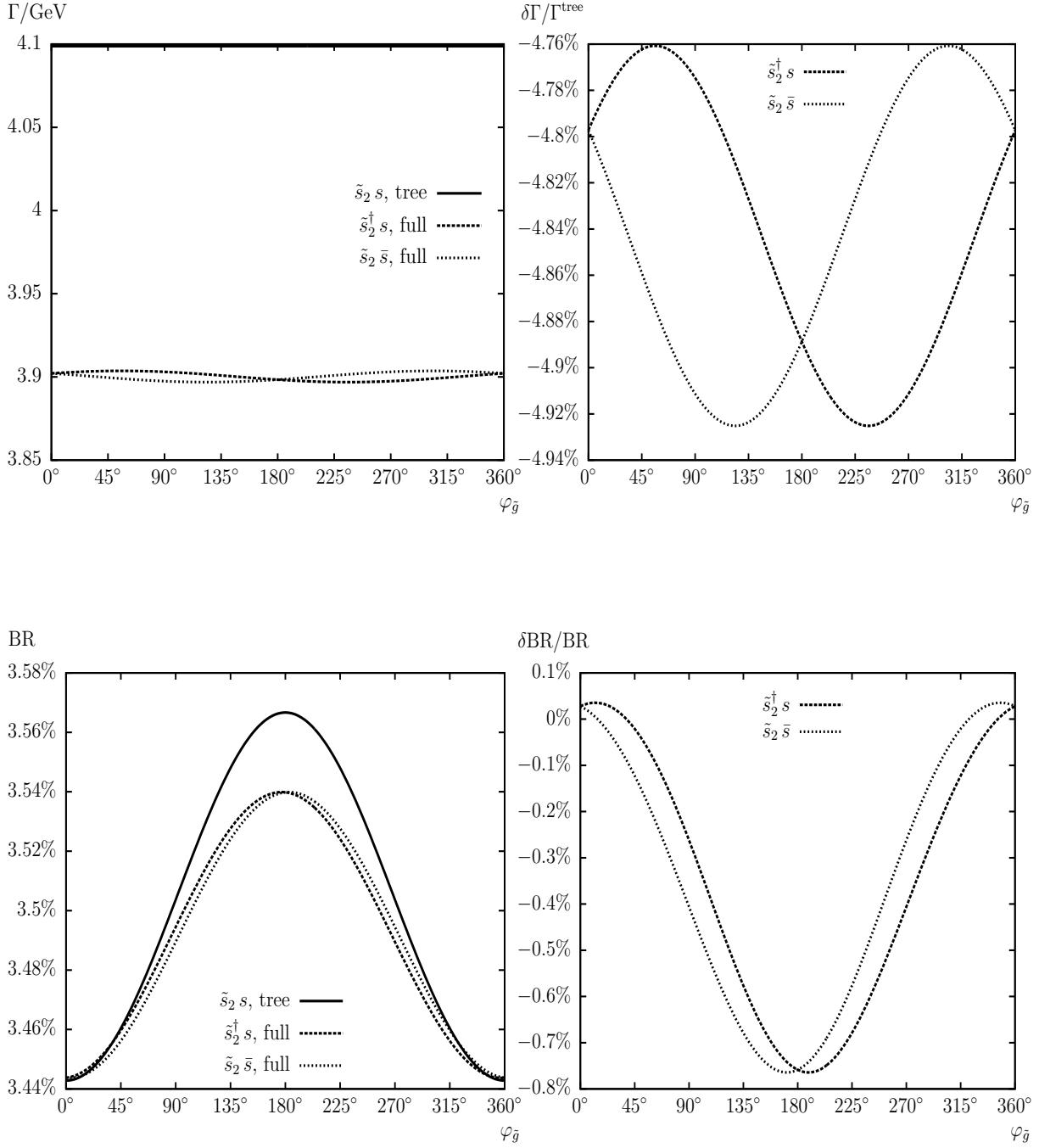


Figure 22: $\Gamma(\tilde{g} \rightarrow \tilde{s}_2 s)$. Tree-level (“tree”) and full one-loop (“full”) corrected decay widths (including absorptive self-energy contributions) are shown. The parameters are chosen according to \mathcal{S} (see Tab. 1), with $\varphi_{\tilde{g}}$ varied. The upper left plot shows the decay width, the upper right plot shows the relative size of the corrections. The lower left plot shows the BR, the lower right plot shows the relative size of the BR.

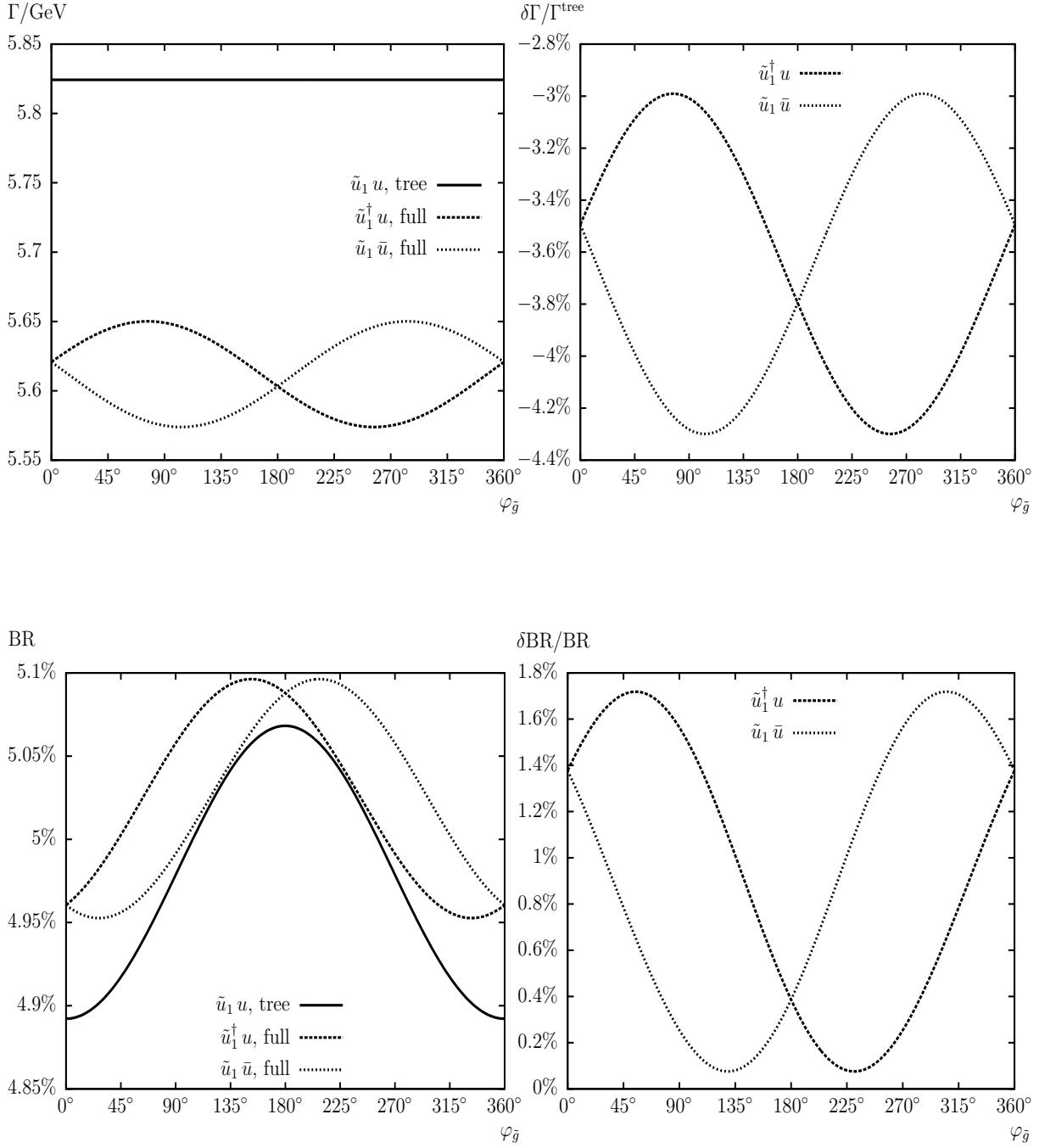


Figure 23: $\Gamma(\tilde{g} \rightarrow \tilde{u}_1 u)$. Tree-level (“tree”) and full one-loop (“full”) corrected decay widths (including absorptive self-energy contributions) are shown. The parameters are chosen according to \mathcal{S} (see Tab. 1), with $\varphi_{\tilde{g}}$ varied. The upper left plot shows the decay width, the upper right plot shows the relative size of the corrections. The lower left plot shows the BR, the lower right plot shows the relative size of the BR.

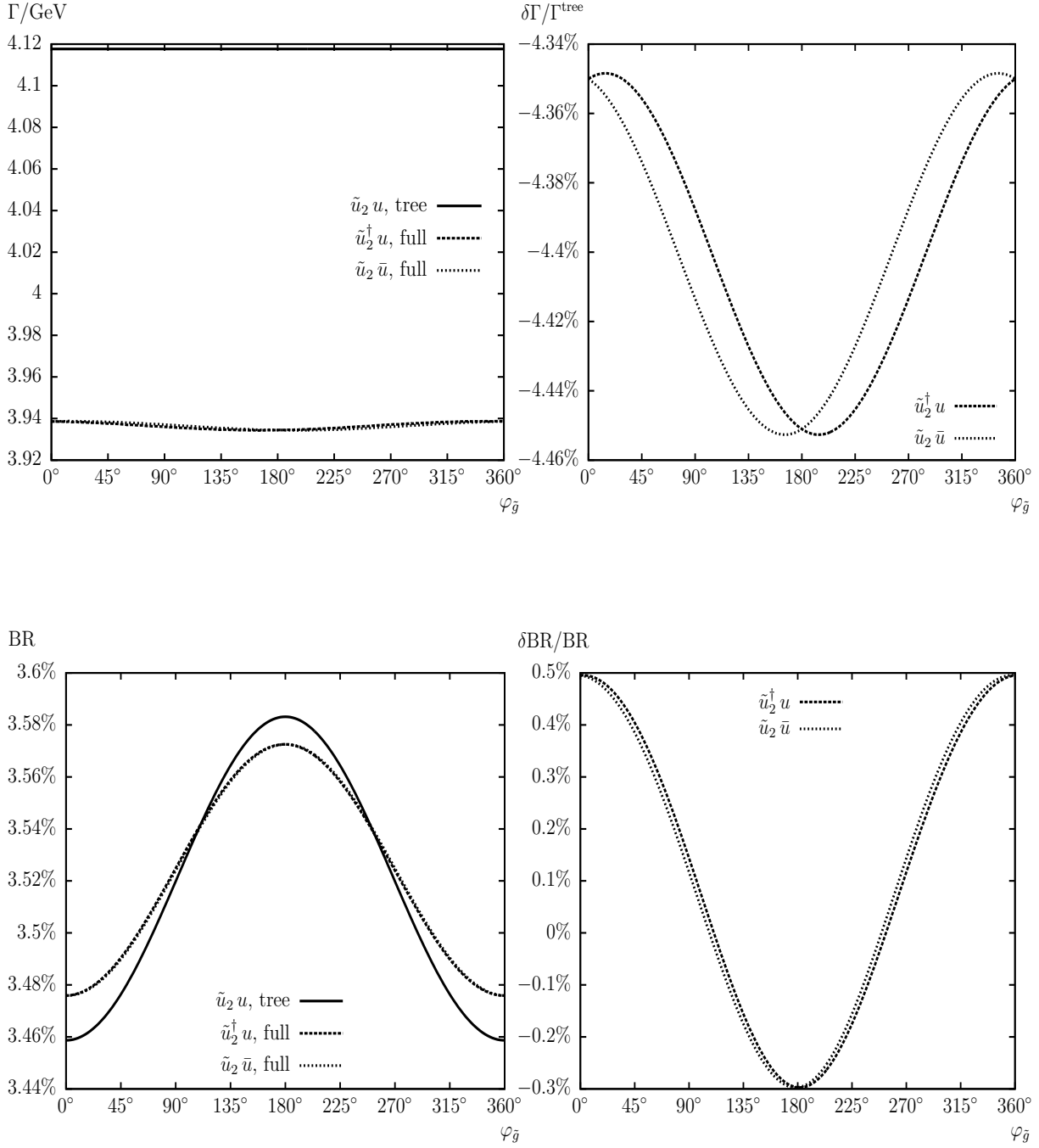


Figure 24: $\Gamma(\tilde{g} \rightarrow \tilde{u}_2 u)$. Tree-level (“tree”) and full one-loop (“full”) corrected decay widths (including absorptive self-energy contributions) are shown. The parameters are chosen according to \mathcal{S} (see Tab. 1), with $\varphi_{\tilde{g}}$ varied. The upper left plot shows the decay width, the upper right plot shows the relative size of the corrections. The lower left plot shows the BR, the lower right plot shows the relative size of the BR.

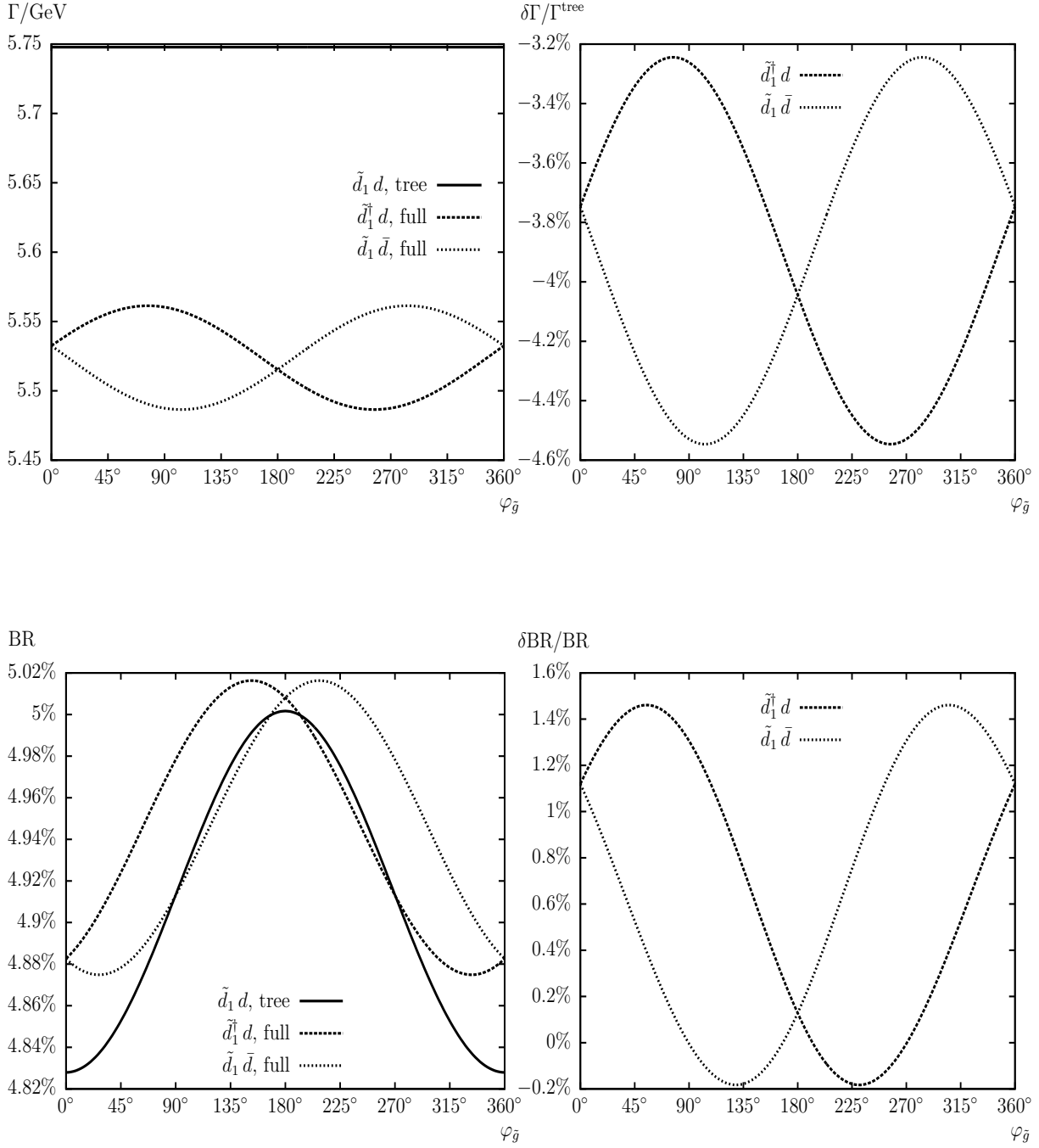


Figure 25: $\Gamma(\tilde{g} \rightarrow \tilde{d}_1 d)$. Tree-level (“tree”) and full one-loop (“full”) corrected decay widths (including absorptive self-energy contributions) are shown. The parameters are chosen according to \mathcal{S} (see Tab. 1), with $\varphi_{\tilde{g}}$ varied. The upper left plot shows the decay width, the upper right plot shows the relative size of the corrections. The lower left plot shows the BR, the lower right plot shows the relative size of the BR.

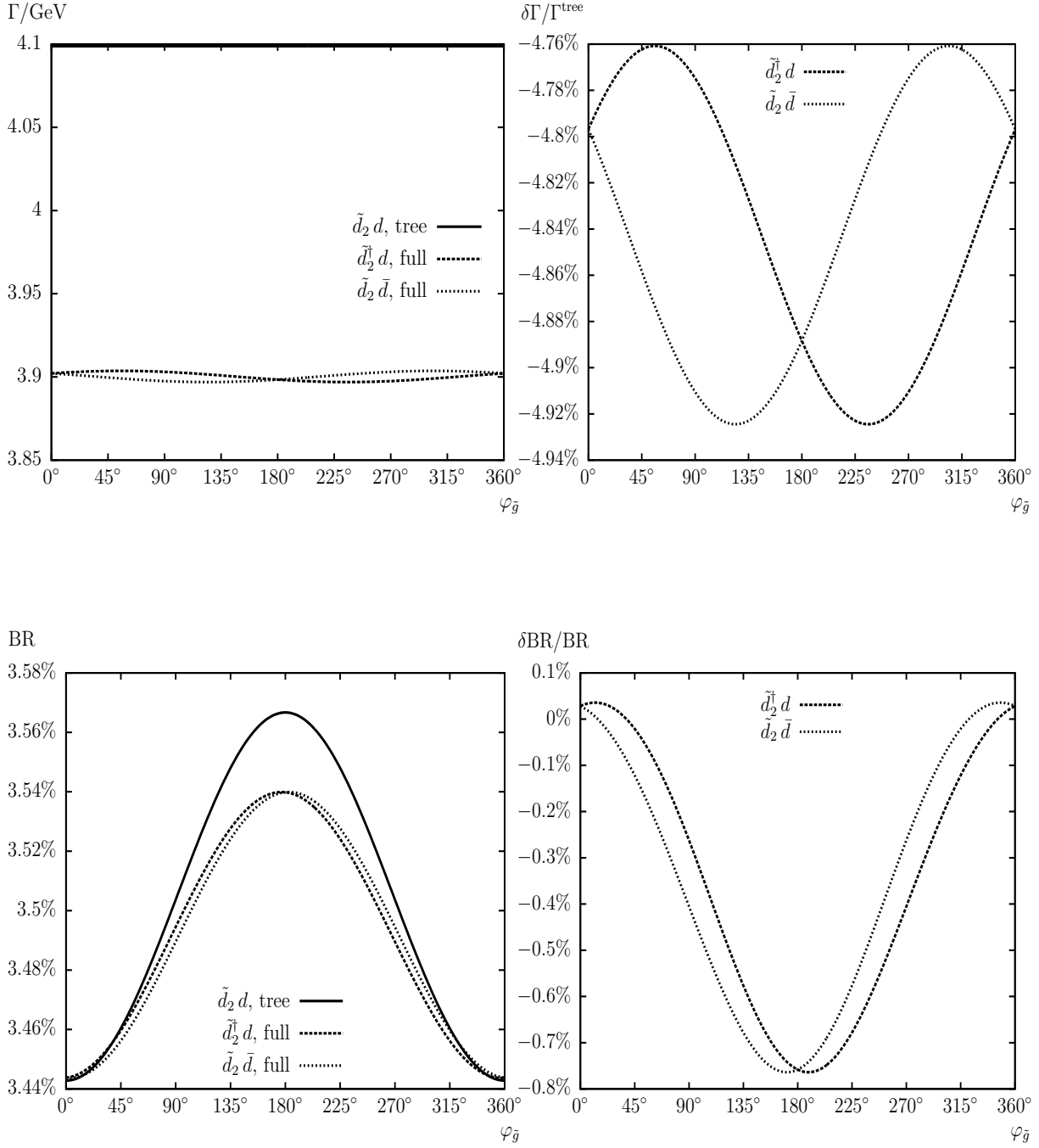


Figure 26: $\Gamma(\tilde{g} \rightarrow \tilde{d}_2 d)$. Tree-level (“tree”) and full one-loop (“full”) corrected decay widths (including absorptive self-energy contributions) are shown. The parameters are chosen according to \mathcal{S} (see Tab. 1), with $\varphi_{\tilde{g}}$ varied. The upper left plot shows the decay width, the upper right plot shows the relative size of the corrections. The lower left plot shows the BR, the lower right plot shows the relative size of the BR.

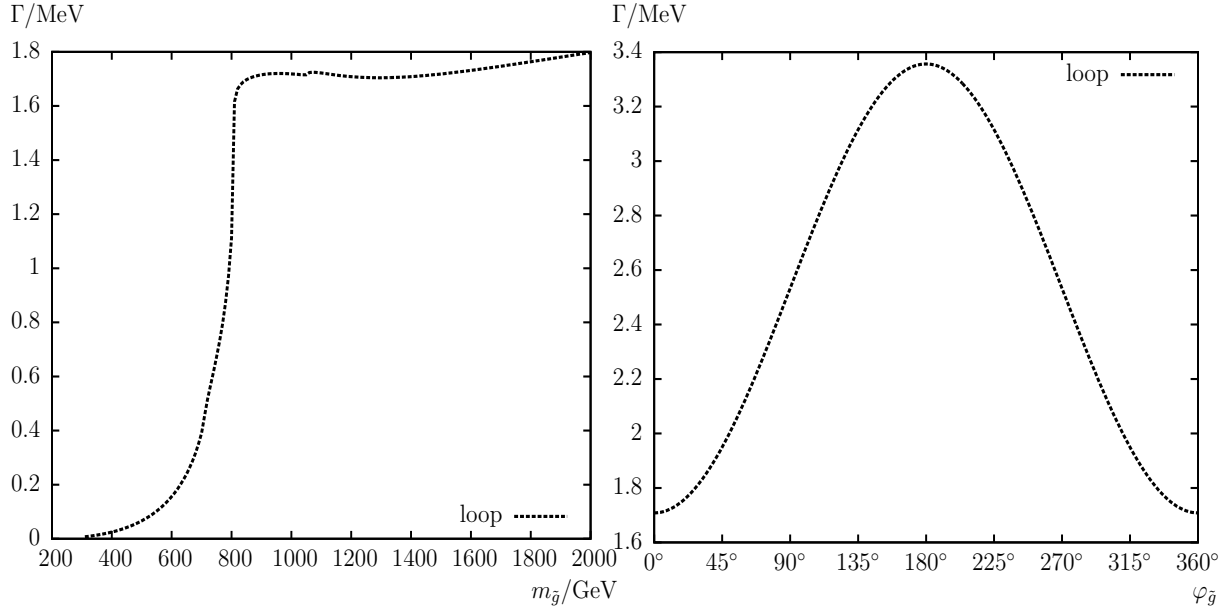


Figure 27: $\Gamma(\tilde{g} \rightarrow \tilde{\chi}_1^0 g)$. One-loop (“loop”) corrected decay widths are shown with the parameters chosen according to \mathcal{S} (see Tab. 1), with $m_{\tilde{g}}$ (left plot) and $\varphi_{\tilde{g}}$ (right plot) varied.

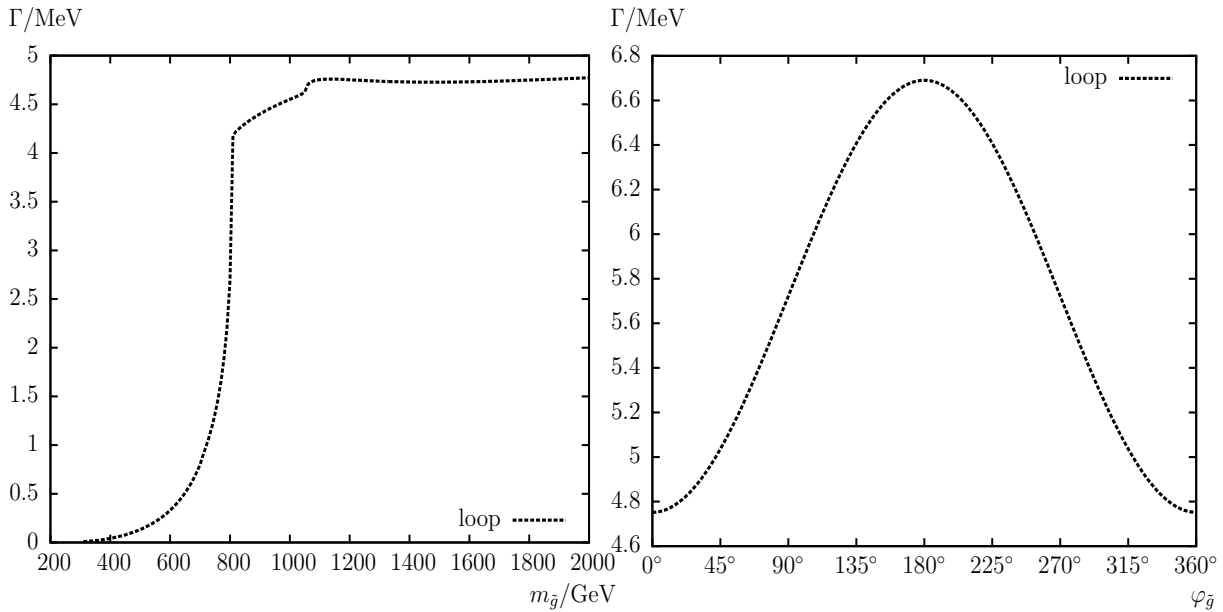


Figure 28: $\Gamma(\tilde{g} \rightarrow \tilde{\chi}_2^0 g)$. One-loop (“loop”) corrected decay widths are shown with the parameters chosen according to \mathcal{S} (see Tab. 1), with $m_{\tilde{g}}$ (left plot) and $\varphi_{\tilde{g}}$ (right plot) varied.

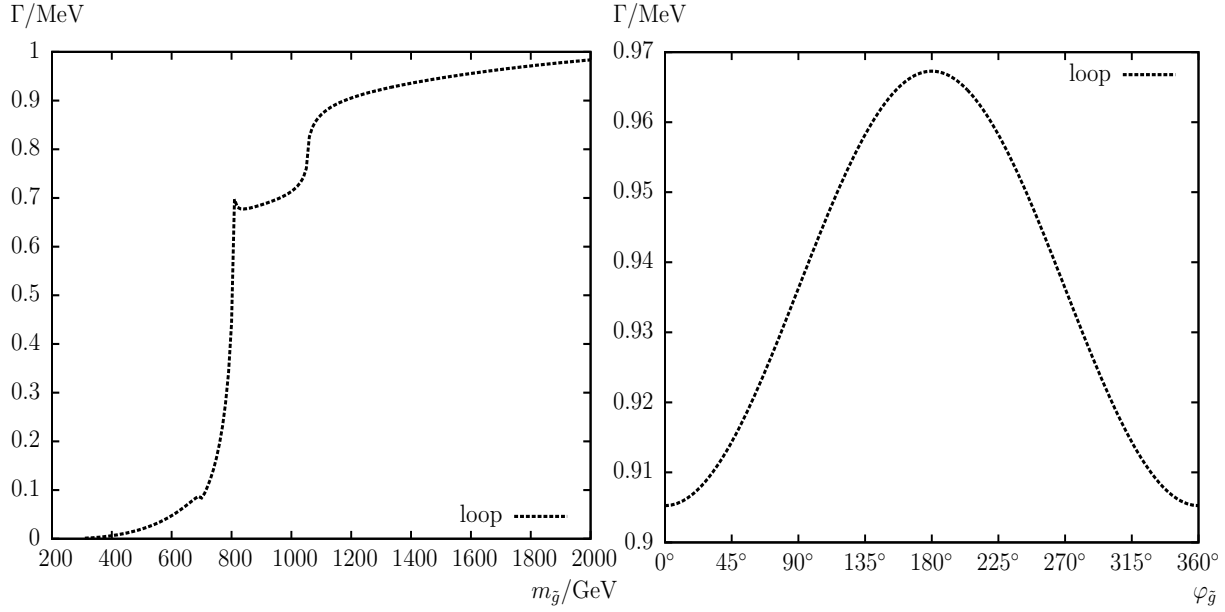


Figure 29: $\Gamma(\tilde{g} \rightarrow \tilde{\chi}_3^0 g)$. One-loop (“loop”) corrected decay widths are shown with the parameters chosen according to \mathcal{S} (see Tab. 1), with $m_{\tilde{g}}$ (left plot) and $\varphi_{\tilde{g}}$ (right plot) varied.

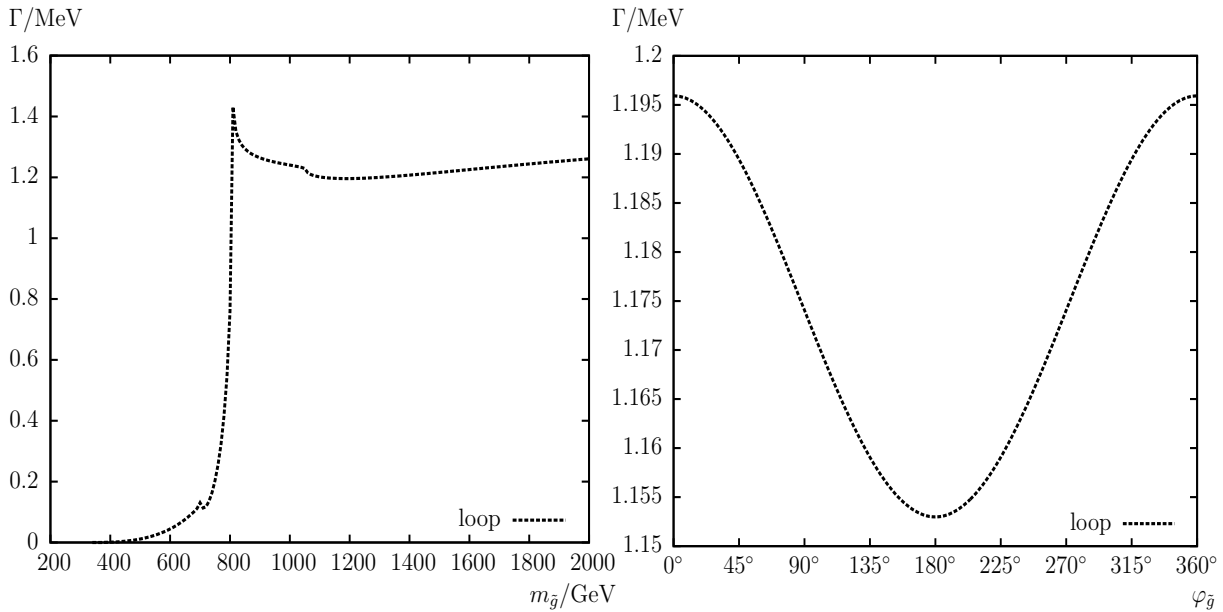


Figure 30: $\Gamma(\tilde{g} \rightarrow \tilde{\chi}_4^0 g)$. One-loop (“loop”) corrected decay widths are shown with the parameters chosen according to \mathcal{S} (see Tab. 1), with $m_{\tilde{g}}$ (left plot) and $\varphi_{\tilde{g}}$ (right plot) varied.

4.5 The total decay width

Finally we show the results for the total decay width of the gluino, see Eqs. (41). In Fig. 31 the upper panels show the absolute and relative variation with $m_{\tilde{g}}$. We observe a nearly linear rise from the threshold region on up to $m_{\tilde{g}} = 2$ TeV, where $\Gamma_{\text{tot}} \approx 370$ GeV is reached. The relative size of the corrections are around +15% close to the production threshold, reaches -10% at $m_{\tilde{g}} = 800$ GeV and levels out at $\sim -2.5\%$ for large gluino masses. Depending on the choice of SUSY parameters and the location of (production) thresholds the size of the one-loop corrections are non-negligible at the LHC. We also included here the pure SQCD corrections, which tend to overestimate the full result by $\sim -5\%$ at low $m_{\tilde{g}}$ and go to zero at large $m_{\tilde{g}}$, where the EW corrections are dominating.

The lower panels of Fig. 31 show the result as a function of $\varphi_{\tilde{g}}$. For the nominal value of $m_{\tilde{g}} = 1200$ GeV we find the loop-corrected total decay width between ~ 113 GeV for $\varphi_{\tilde{g}} = 0^\circ$ and ~ 110 GeV for $\varphi_{\tilde{g}} = 180^\circ$. The relative size of the corrections vary between -4.8% and -4.2%, possibly still relevant for LHC measurements.

5 Conclusions

We have evaluated all two-body decay widths of the gluino in the Minimal Supersymmetric Standard Model with complex parameters (cMSSM). The decay modes are given in Eqs. (1) – (3). After the (pair) production of gluinos they are expected to decay via cascades to lighter SUSY particles and quarks and/or leptons. Consequently, the decay of a gluino to a scalar quark and a quark will one of the most relevant decays in such a cascade. In order to determine the masses, couplings and parameters of SUSY particles precisely in such cascades, higher-order corrections are necessary to keep the theory error on an acceptable level.

Our evaluation is based on a full one-loop calculation of all decay channels, also including soft and hard QED and QCD radiation, necessary to derive a reliable prediction of any two-body branching ratio. We also include the purely loop induced decays $\tilde{g} \rightarrow \tilde{\chi}_k^0 g$ ($k = 1, 2, 3, 4$). These modes as well as possible three-body decay modes can become sizable only if all the two-body channels are kinematically (nearly) closed. We have not investigated these three-body decay modes, which are, beyond the scope of this paper.

We first reviewed the relevant sectors of the cMSSM, including their renormalization (where extensive explanations can be found in Refs. [15, 16, 27]). We have discussed the calculation of the one-loop diagrams, the treatment of UV- and IR-divergences (where the latter are canceled by the inclusion of real soft QCD and QED radiation), and in addition the hard QCD and QED bremsstrahlung.

For the numerical analysis we have chosen one parameter set that allows simultaneously *all* two-body decay modes and respect the current experimental bounds on Higgs boson and SUSY searches. In a first step we have shown the results as a function of $m_{\tilde{g}}$. For the largest value included in our analysis, $m_{\tilde{g}} = 2$ TeV we find decay widths of ~ 15 GeV, and $\text{BR}(\tilde{g} \rightarrow \tilde{q}_1 q) + \text{BR}(\tilde{g} \rightarrow \tilde{q}_2 q) \sim 1/6$. The largest deviations were found for the decays involving the third generation (s)quarks, where effects of the squark mixing and corresponding changes in the masses and couplings are maximal. The size of the one-loop corrections is found to be largest close to the production thresholds and reaches several per-cent for large $m_{\tilde{g}}$. We have also investigated the quality of the approximation of the

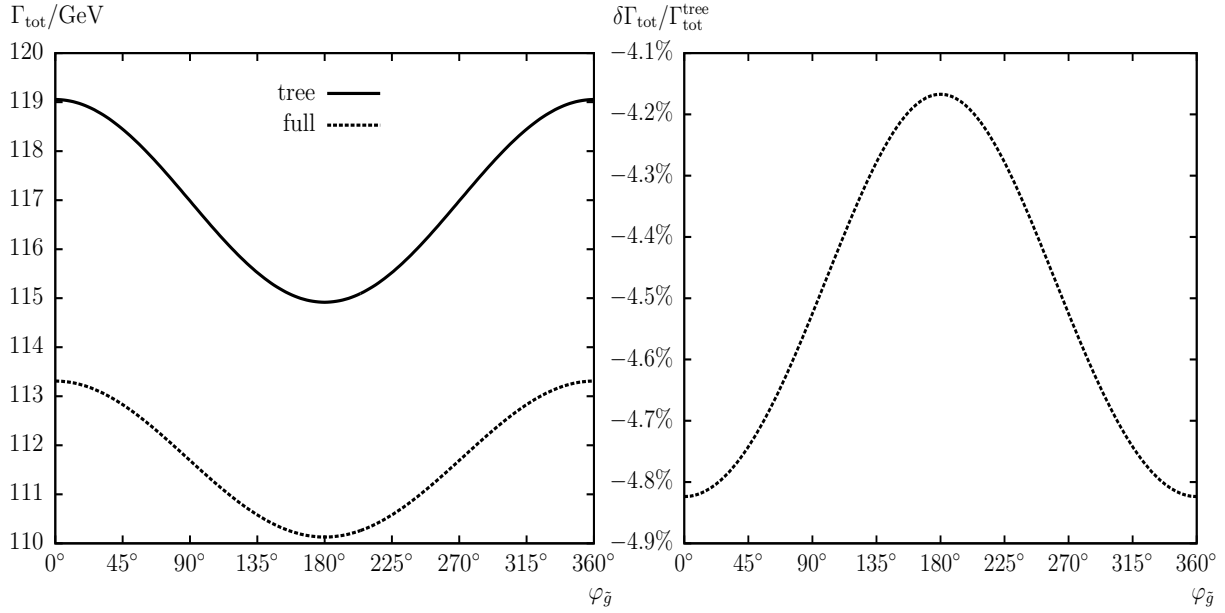
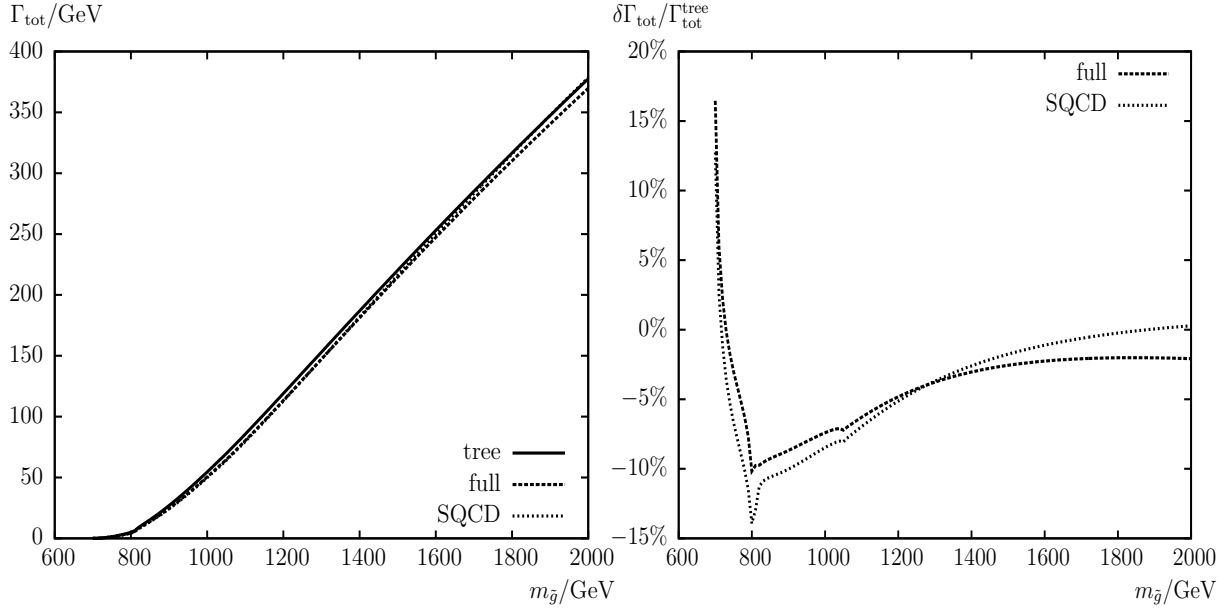


Figure 31: Γ_{tot} . Tree-level (“tree”), full one-loop (“full”) and pure SQCD (“SQCD”) corrected decay widths are shown with the parameters chosen according to \mathcal{S} (see Tab. 1). The upper left plot shows the total decay width, the upper right plot shows the relative size of the total corrections, with $m_{\tilde{g}}$ varied. The lower plots show the same but with $\varphi_{\tilde{g}}$ varied (including absorptive self-energy contributions).

pure SQCD corrections. While for some channels, especially involving lighter quarks, the SQCD contributions yield a good approximation, in the channels involving scalar tops and bottoms the EW corrections, which were evaluated here for the first time, are crucial to yield a reliable result.

In a second step we have analyzed the dependence of the decay widths and branching ratios on the phase of the gluino mass parameter, $\varphi_{\tilde{g}}$, for $m_{\tilde{g}} = 1200$ GeV fixed. Again, the results are to a large extent flavor independent, except for decays involving (scalar) tops. In the latter case a variation of the BR of up to 14% was found, and the size of the loop corrections can yield $\sim 10\%$. For the other flavors we find as before $\text{BR}(\tilde{g} \rightarrow \tilde{q}_1 q) + \text{BR}(\tilde{g} \rightarrow \tilde{q}_2 q) \sim 1/6$, and a smaller variation with $\varphi_{\tilde{g}}$.

The size of the widths of the purely loop-induced decays is substantially smaller, staying below 0.01 GeV for our parameters. This could change if the gluino were lighter than all scalar quarks. In that case also three-body decays would be relevant, which, however, were not investigated here.

Furthermore, it has to be kept in mind that we have evaluated the full one-loop corrections for one set of parameters only, which was chosen to have many decay modes open, and *not* to emphasize the loop corrections. Consequently, it can easily be imagined that substantially larger or smaller corrections can be found for other choices of SUSY parameters. The full one-loop corrections should (eventually) be taken into account in precision analyses of cascade decays at the LHC. Nevertheless, the size of the loop corrections found give an idea of the relevance of the full one-loop corrections.

Following our analysis it is evident that the full one-loop corrections are mandatory for a precise prediction of the various branching ratios. The results for the gluino decays will be implemented into the Fortran code `FeynHiggs`.

Acknowledgements

We thank A. Denner, T. Hahn, F. von der Pahlen, H. Rzehak and G. Weiglein for helpful discussions. We thank also S. Liebler for his help by the implementation of the photon bremsstrahlung. The work of S.H. was partially supported by CICYT (grant FPA 2010–22163-C02-01) and by the Spanish MICINN’s Consolider-Ingenio 2010 Program under grant MultiDark CSD2009-00064.

References

- [1] H.P. Nilles, *Phys. Rept.* **110** (1984) 1;
H.E. Haber and G.L. Kane, *Phys. Rept.* **117** (1985) 75;
R. Barbieri, *Riv. Nuovo Cim.* **11** (1988) 1.
- [2] G. Aad et al. [The ATLAS Collaboration], arXiv:0901.0512.
- [3] G. Bayatian et al. [CMS Collaboration], *J. Phys.* **G 34** (2007) 995.
- [4] O. Buchmueller et al., *Eur. Phys. J. C* **64** (2009) 391 [arXiv:0907.5568 [hep-ph]].

- [5] W. Beenakker, R. Höpker and P. Zerwas, *Phys. Lett. B* **378** (1996) 159 [arXiv:hep-ph/9602378].
- [6] M. Mühlleitner, A. Djouadi and Y. Mambrini, *Comput. Phys. Commun.* **168** (2005) 46 [arXiv:hep-ph/0311167].
- [7] S. Choi, M. Drees, A. Freitas and P. Zerwas, *Phys. Rev. D* **78** (2008) 095007 [arXiv:0808.2410 [hep-ph]].
- [8] M. Krämer, E. Popenza, M. Spira and P. Zerwas, *Phys. Rev. D* **80** (2009) 055002 [arXiv:0902.3795 [hep-ph]].
- [9] A. De Roeck et al., *Eur. Phys. J. C* **66** (2010) 525 [arXiv:0909.3240 [hep-ph]].
- [10] S. Heinemeyer, W. Hollik and G. Weiglein, *Comput. Phys. Commun.* **124** (2000) 76 [arXiv:hep-ph/9812320]; see www.feynhiggs.de.
- [11] S. Heinemeyer, W. Hollik and G. Weiglein, *Eur. Phys. J. C* **9** (1999) 343 [arXiv:hep-ph/9812472].
- [12] G. Degrandi, S. Heinemeyer, W. Hollik, P. Slavich and G. Weiglein, *Eur. Phys. J. C* **28** (2003) 133 [arXiv:hep-ph/0212020].
- [13] M. Frank, T. Hahn, S. Heinemeyer, W. Hollik, R. Rzehak and G. Weiglein, *JHEP* **02** (2007) 047 [arXiv:hep-ph/0611326].
- [14] T. Fritzsche, PhD thesis, Cuvillier Verlag, Göttingen 2005, ISBN 3–86537–577–4.
- [15] S. Heinemeyer, H. Rzehak and C. Schappacher, *Phys. Rev. D* **82** (2010) 075010 [arXiv:1007.0689 [hep-ph]];
PoS C **CHARGED2010** (2010) 039 [arXiv:1012.4572 [hep-ph]].
- [16] T. Fritzsche, S. Heinemeyer, H. Rzehak and C. Schappacher, arXiv:1111.7289 [hep-ph].
- [17] A. Fowler and G. Weiglein, *JHEP* **1001** (2010) 108 [arXiv:0909.5165 [hep-ph]].
- [18] A. Denner, *Fortsch. Phys.* **41** (1993) 307 [arXiv:0709.1075 [hep-ph]].
- [19] K. Nakamura et al. [Particle Data Group], *J. Phys. G* **37** (2010) 075021.
- [20] K. Chetyrkin, J. Kühn and M. Steinhauser, *Comput. Phys. Commun.* **133** (2000) 43 [arXiv:hep-ph/0004189].
- [21] R. Hempfling, *Phys. Rev. D* **49** (1994) 6168;
L. Hall, R. Rattazzi and U. Sarid, *Phys. Rev. D* **50** (1994) 7048 [arXiv:hep-ph/9306309];
M. Carena, M. Olechowski, S. Pokorski and C. Wagner, *Nucl. Phys. B* **426** (1994) 269 [arXiv:hep-ph/9402253].
- [22] M. Carena, D. Garcia, U. Nierste and C. Wagner, *Nucl. Phys. B* **577** (2000) 577 [arXiv:hep-ph/9912516].

- [23] R. Harlander, L. Mihaila and M. Steinhauser, *Phys. Rev. D* **72** (2005) 095009 [arXiv:hep-ph/0509048].
- [24] R. Peccei and H. Quinn, *Phys. Rev. Lett.* **38** (1977) 1440; *Phys. Rev. D* **16** (1977) 1791.
- [25] S. Dimopoulos and S. Thomas, *Nucl. Phys. B* **465** (1996) 23 [arXiv:hep-ph/9510220].
- [26] J. Küblbeck, M. Böhm and A. Denner, *Comput. Phys. Commun.* **60** (1990) 165; T. Hahn, *Comput. Phys. Commun.* **140** (2001) 418 [arXiv:hep-ph/0012260]; T. Hahn and C. Schappacher, *Comput. Phys. Commun.* **143** (2002) 54 [arXiv:hep-ph/0105349].
The program, the user's guide and the MSSM model files are available via www.feynarts.de.
- [27] S. Heinemeyer, F. v.d. Pahlen and C. Schappacher, arXiv:1112.0760 [hep-ph].
- [28] T. Hahn and M. Pérez-Victoria, *Comput. Phys. Commun.* **118** (1999) 153 [arXiv:hep-ph/9807565].
- [29] F. del Aguila, A. Culatti, R. Munoz Tapia and M. Perez-Victoria, *Nucl. Phys. B* **537** (1999) 561 [arXiv:hep-ph/9806451].
- [30] W. Siegel, *Phys. Lett. B* **84** (1979) 193; D. Capper, D. Jones, and P. van Nieuwenhuizen, *Nucl. Phys. B* **167** (1980) 479.
- [31] D. Stöckinger, *JHEP* **0503** (2005) 076 [arXiv:hep-ph/0503129].
- [32] W. Hollik and D. Stöckinger, *Phys. Lett. B* **634** (2006) 63 [arXiv:hep-ph/0509298].
- [33] The couplings can be found in the files `MSSM.ps.gz` and `MSSMQCD.ps.gz` as part of the `FeynArts` package [26].
- [34] [LEP Higgs working group], *Phys. Lett. B* **565** (2003) 61 [arXiv:hep-ex/0306033].
- [35] [LEP Higgs working group], *Eur. Phys. J. C* **47** (2006) 547 [arXiv:hep-ex/0602042].
- [36] V. Khachatryan et al. [CMS Collaboration], arXiv:1101.1628 [hep-ex]; <http://cdsweb.cern.ch/record/1342547/files/SUS-11-001-pas.pdf>; <http://cdsweb.cern.ch/record/1343076/files/SUS-10-005-pas.pdf>; G. Aad et al. [ATLAS Collaboration], arXiv:1102.2357 [hep-ex]; arXiv:1102.5290 [hep-ex].
- [37] J. Frere, D. Jones and S. Raby, *Nucl. Phys. B* **222** (1983) 11; M. Claudson, L. Hall and I. Hinchliffe, *Nucl. Phys. B* **228** (1983) 501; C. Kounnas, A. Lahanas, D. Nanopoulos and M. Quiros, *Nucl. Phys. B* **236** (1984) 438; J. Gunion, H. Haber and M. Sher, *Nucl. Phys. B* **306** (1988) 1; J. Casas, A. Lleyda and C. Munoz, *Nucl. Phys. B* **471** (1996) 3 [arXiv:hep-ph/9507294]; P. Langacker and N. Polonsky, *Phys. Rev. D* **50** (1994) 2199 [arXiv:hep-ph/9403306]; A. Strumia, *Nucl. Phys. B* **482** (1996) 24 [arXiv:hep-ph/9604417].

- [38] M. Dugan, B. Grinstein and L. Hall, *Nucl. Phys.* **B 255** (1985) 413.
- [39] W. Hollik, J. Illana, S. Rigolin and D. Stöckinger, *Phys. Lett.* **B 416** (1998) 345 [arXiv:hep-ph/9707437]; *Phys. Lett.* **B 425** (1998) 322 [arXiv:hep-ph/9711322].
- [40] D. Demir, O. Lebedev, K. Olive, M. Pospelov and A. Ritz, *Nucl. Phys.* **B 680** (2004) 339 [arXiv:hep-ph/0311314].
- [41] D. Chang, W. Keung and A. Pilaftsis, *Phys. Rev. Lett.* **82** (1999) 900 [Erratum-ibid. **83** (1999) 3972] [arXiv:hep-ph/9811202];
A. Pilaftsis, *Phys. Lett.* **B 471** (1999) 174 [arXiv:hep-ph/9909485].
- [42] O. Lebedev, K. Olive, M. Pospelov and A. Ritz, *Phys. Rev.* **D 70** (2004) 016003 [arXiv:hep-ph/0402023].
- [43] S. Abel, S. Khalil and O. Lebedev, *Nucl. Phys.* **B 606** (2001) 151 [arXiv:hep-ph/0103320].
- [44] Y. Li, S. Profumo and M. Ramsey-Musolf, *JHEP* **1008** (2010) 062 [arXiv:1006.1440 [hep-ph]].